Journal of Inorganic and Organometallic Polymers and Materials (2025) 35:5509–5530
https://doi.org/10.1007/s10904-025-03605-x

RESEARCH

Adsorption-Assisted Photocatalytic Degradation of Anionic Direct Yellow-50 and Cationic Methylene Blue Dyes by Chemically Synthesized Poly(1,5-diaminoanthraquinone)

Aleyna Akıllı[1] · Ayşenur Özler[1] · Bircan Haspulat Taymaz[1] · Ahmet Hancı[1] · Volkan Eskizeybek[2] · Handan Kamış[1]

Received: 20 December 2024 / Accepted: 8 January 2025 / Published online: 16 January 2025

Abstract
Conducting polymers renowned for their exceptional photocatalytic activity, conductivity, and visible-light absorption capabilities present a compelling alternative for advanced photocatalytic applications. In this regard, the creation of conductive polymers of the next generation has enormous promise for improving energy efficiency as well as solving environmental issues. In this study, the conductive polymer poly(1,5-diaminoanthraquinone) (PDAAQ) with a band gap of 1.28 eV and an electrical conductivity of 1.23 S/cm was successfully synthesized via chemical oxidative polymerization using ammonium peroxydisulfate as an oxidant and perchloric acid as an initiator in an acetonitrile polymerization medium. The adsorption-assisted photocatalytic performance of PDAAQ has been investigated in cationic methylene blue (MB) and an anionic direct yellow (DY) dye under visible irradiation. The effect of polymerization medium, oxidant type, polymerization time, and monomer oxidant ratio on adsorption-assisted photocatalytic degradation of MB was investigated. The synthesized PDAAQ polymer demonstrates exceptional photocatalytic performance, completely degrading MB and DYE dyes under visible light illumination in 6 and 8 min through an adsorption-assisted photocatalysis mechanism. Besides, the photocatalytic dye degradation performance of PDAAQ was investigated for the degradation of synthetic wastewater (SWW) under visible light. The PDAAQ polymer proves to be an effective photocatalyst for photocatalytic applications, showcasing exceptional potential in degrading model dyes and treating synthetic wastewater.

Keywords Conductive polymer · Poly(1,5-diaminoanthraquinone) · Chemical oxidative polymerization · Photocatalytic dye degradation

1 Introduction

Water contamination has become a critical global issue due to population growth and the rising demands of industrial and agricultural activities. Industrial wastewater, particularly from the textile sector, poses significant environmental threats, including harm to aquatic life, potential animal injuries, and disruption of underwater photosynthesis caused by sunlight blockage [1, 2]. Therefore, to reduce these environmental risks, such effluent must be treated [3].

Different techniques are used in wastewater treatment to discharge treated water safely. Biological treatment [4], filtration [5], absorption/adsorption [6], and membrane processes [7, 8] are a few examples of these procedures. Traditional wastewater treatment techniques often fail to eliminate organic pollutants and heavy metals effectively. Photocatalysis has emerged globally as a sustainable and efficient alternative for wastewater treatment due to its practicality, non-selective nature, and reusability of photocatalyst [7, 9]. This approach enables the breakdown of complex pollutants into simpler substances such as water, carbon dioxide, and inorganic ions [10]. Photocatalysis is recognized as one of the most effective techniques for the

✉ Bircan Haspulat Taymaz
bhaspulat@ktun.edu.tr

✉ Handan Kamış
hkamis@ktun.edu.tr

[1] Department of Chemical Engineering, Konya Technical University, 42250 Konya, Turkey

[2] Department of Materials Science and Engineering, Çanakkale Onsekiz Mart University, 17020 Çanakkale, Turkey

mineralization of complex contaminants, offering a viable alternative for breaking down and eliminating pollutants [11, 12]. Ideal photocatalytic materials should be low-cost, non-toxic, composed of a range of raw materials, highly efficient, stable, easy to separate and recover, and capable of absorbing visible light [13, 14]. Conducting polymers have emerged as promising alternatives to conventional photocatalysts due to their exceptional photocatalytic activity, excellent conductivity, unique optical properties, and small band gaps that facilitate visible light absorption [15, 16]. Additionally, electroconductivity, electrocatalysis, electroactivity, optical activity, and ion adsorption can be readily controlled through a reversible doping/dedoping process. The conducting polymers polyaniline (PANI) [3, 17, 18], poly (3,4-ethylene dioxythiophene) (PEDOT) [19], polypyrrole (PPy) [20], polythiophene (PTH) [21], and their derivatives are frequently employed in photocatalytic wastewater treatment applications. Abdiryim et al. evaluated the photocatalytic degradation efficiency of pure PEDOT (poly(3,4-ethylenedioxythiophene)) for methylene blue (MB) dye under UV and natural sunlight irradiation. Pure PEDOT achieved a degradation efficiency of 37.7% under UV light and 33.9% under natural sunlight within 5 h. This study highlights that pure PEDOT exhibits moderate photocatalytic activity for degrading organic dyes, with performance depending on the light source and exposure duration [22] Ahmad et al. conducted a study in 2020 using pure polypyrrole (PPy) for the photocatalytic degradation of Direct Yellow dye. The study reported that PPy achieved a 65% degradation efficiency under visible light within 180 min [23].

PANI is a well-known conductive polymer with its chemical stability, low cost, high conductivity, simple production process, and strong redox characteristics. Haspulat Taymaz et al. investigated the photocatalytic activity of pure polyaniline (PANI) films for dye degradation. Pure PANI achieved 63% degradation efficiency for methylene blue (MB) and 79% for rhodamine B (RdB) under UV light within 30 min. Under visible light, the degradation efficiencies were 39% for MB and 52% for RdB after the same duration. This demonstrates that PANI shows moderate photocatalytic activity, with higher efficiency under UV light compared to visible light [24]. Although PANI is a well-known conductive polymer [3] with many benefits, its instability can eventually cause conductivity to decrease, particularly when exposed to environmental elements like oxygen and moisture [25]. PANI needs dopants to increase their conductivity; however, the efficacy of these dopants varies, and performance may be hampered by poor selection [26]. While the synthesis of polyaniline (PANI) can be complex, making large-scale production with high purity challenging [27], PDAAQ offers an alternative as a conductive polymer with exceptional electroactivity and stability, which is attributed to the integration of a polyaniline skeleton and a 1,4-benzoquinone moiety [28]. PDAAQ features a 1,4-benzoquinone moiety condensed between two aniline groups, resulting in enhanced electroactivity and stability compared to polyaniline due to its hybridized structure. The quinone ($Q/Q^{\cdot -}/Q^{2-}$) group in the π-conjugated system provides superior electroactivity, surpassing other conducting polymers. Additionally, the supramolecular structure of PDAAQ, reinforced by strong π-conjugated interactions between anthracene rings and hydrogen bonds between N-H and C=O groups, ensures superior cycle stability compared to other known conductive polymers [29].

The synthesis of PDAAQs has garnered attention in recent years [28–30]. The electropolymerization of PDAAQs leads to the improved electrochemical performance of the polymer [29, 31, 32]; however, large-scale production remains impractical. Typically, PDAAQ is synthesized through chemical oxidative polymerization using oxidizing agents like ammonium persulfate or potassium permanganate [33], facilitating the oxidation of the monomer and forming PDAAQ with a conjugated structure. This method allows for customizing PDAAQ properties, such as conductivity and stability, by adjusting reaction parameters like oxidant concentration and reaction time. Additionally, the process can be conducted at very low temperatures, making it suitable for a wide range of applications [34]. PDAAQ has attracted significant attention as an electrode material for supercapacitors, with the interaction between PDAAQ and conductive frameworks playing a crucial role in enhancing the electrochemical performance of flexible devices [29–31]. However, in existing literature, poly(1,5-diaminoanthraquinone) has not been explored as a photocatalyst. Given its extended π-conjugated system, PDAAQ is expected to absorb light in visible and UV regions, sharing structural similarities with PANI. This broad absorption spectrum would enable PDAAQ to be effectively excited by visible light, positioning it as a promising candidate for photocatalytic applications. Like PANI, PDAAQ may offer similar advantages in light-driven reactions, opening new avenues for research in photocatalytic devices.

The present study synthesized PDAAQ via chemical oxidative polymerization and explored it for the first time as a photocatalyst for removing anionic DY and cationic MB dyes. The synthesized PDAAQ was characterized using a variety of techniques, including Scanning Electron Microscopy (SEM), SEM-Energy Dispersive X-ray Spectroscopy (EDX), X-ray diffraction (XRD), Fourier-Transform Infrared Spectroscopy (FTIR), UV-Vis absorption spectroscopy, and Braeuer-Emmett-Teller (BET) surface area analysis. These methods provided valuable insights into the structural, morphological, and optical properties of PDAAQ,

which are critical to its photocatalytic performance. The photocatalytic efficiency of PDAAQ was evaluated for both anionic and cationic dyes, considering factors such as pH, photocatalyst dosage, dye concentration, and catalyst reusability. The results showed that PDAAQ exhibited significant photocatalytic degradation for both dye types.

Additionally, the adsorption behavior of PDAAQ towards the dyes was examined through dark storage experiments, revealing that adsorption played an essential role in enhancing photocatalytic efficiency. Therefore, the improved photocatalytic activity of PDAAQ can be attributed to its intrinsic photocatalytic properties and high adsorption capacity. To further explore the impact of environmental factors on adsorption-assisted photocatalytic performance, synthetic wastewater containing various ionic species was prepared. The kinetic behavior of dye degradation in this system was studied, shedding light on the influence of different ions on the adsorption-assisted photocatalytic process. Finally, degradation kinetics were also analyzed in a mixed-dye system to understand better how PDAAQ performs in more complex wastewater environments. This study underscores the potential of PDAAQ as an effective photocatalyst for wastewater treatment, emphasizing the optimization of its synthesis and the critical role of adsorption in enhancing its performance. The findings contribute to the expanding field of polymer-based photocatalysts and open new possibilities for designing advanced materials for environmental remediation.

2 Experimental

2.1 Materials

To synthesize PDAAQ, the 1,5 diamino anthraquinone (DAAQ, 90%) monomer used was purchased from Alfa Aesar, and perchloric acid ($HClO_4$, 72%) and ammonium peroxodisulphate (APS) $(NH_4)_2S_2O_8$, 99%) were purchased from Merck. Acetonitrile (CH_3CN, 99%) was purchased from Avantor (J.T. Baker). For the dye degradation and SWW (synthetic wastewater) experiment, DY ($C_{35}H_{24}N_6Na_4O_{13}S_4$), MB ($C_{16}H_{18}C_lN_3S$), sodium sulfate ($Na_2SO_4$), and disodium phosphate (Na_2HPO_4) were purchased from Merck. Wheat starch was purchased from a local market in Türkiye. The solution's pH was adjusted using sulfuric acid (H_2SO_4, 98%) and ammonia (NH_3) purchased from Isolab and Tekkim, respectively. For the scavengers experiments, ascorbic acid ($C_6H_8O_6$), ethylenediamine tetraacetic acid ($C_{10}H_{16}N_2O_8$), and isopropanol (C_3H_8O) were purchased from Kimetsan, Merck, and Lachema, respectively. Deionized water was used for washing and experimental studies.

2.2 Synthesis of PDAAQ

In this study, PDAAQ was synthesized by chemically oxidizing DAAQ using APS as an initiating mechanism and $HClO_4$ as an acidic medium (Fig. 1). For this, 60 mg DAAQ (0.25 mmol) was added to 76 mL pure C_2H_3N. It was stirred at 80 °C in a magnetic stirrer heater for one hour. After

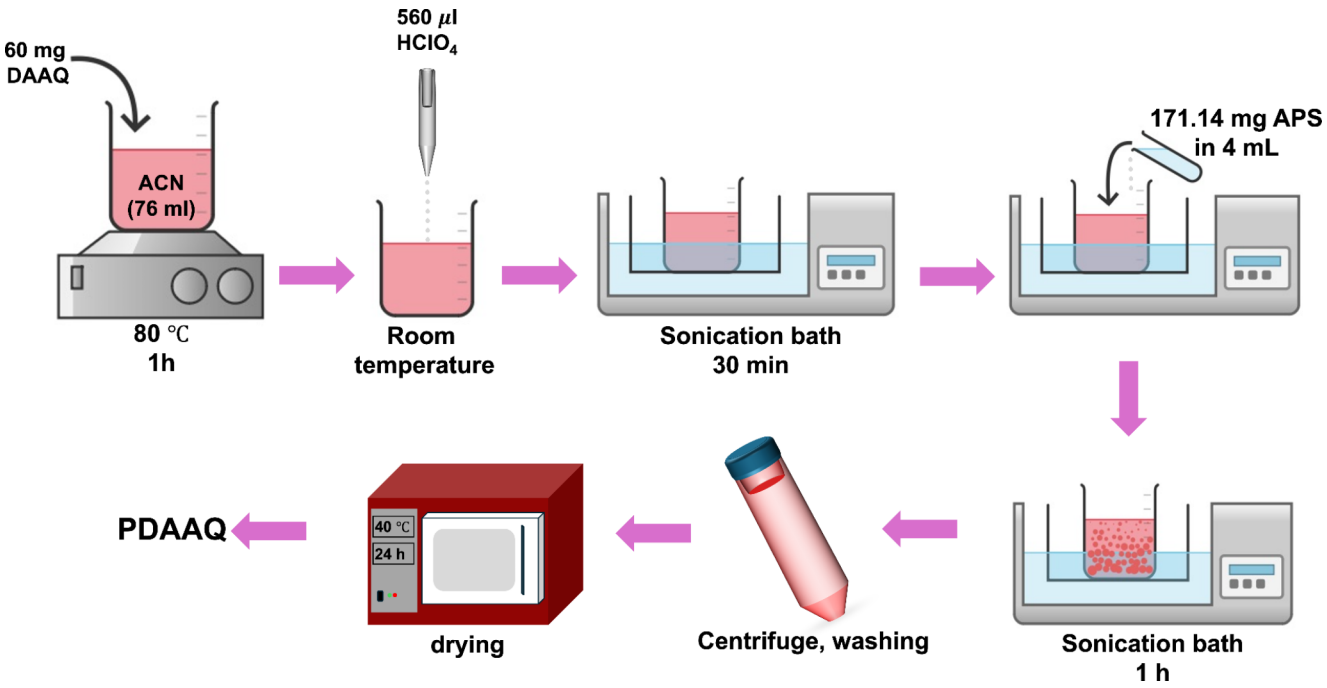

Fig. 1 Synthesis scheme of PDAAQ

cooling to ambient temperature, 560 µL of pure $HClO_4$ was added, and the mixture was sonicated in a sonication bath for 30 min. 171.14 mg APS (0.75 mmol) was dissolved in 4 mL of distilled water and added to the monomer solution. After one hour of sonication, it was washed with ethanol using a centrifuge until the color disappeared. It was dried in a vacuum oven at 40 °C. The effect of polymerization medium, oxidant type, polymerization time, and monomer: oxidant ratio was also investigated.

2.3 Characterization of PDAAQ

The crystalline properties of the polymer were investigated via the X-ray diffraction method (Shimadzu XRD-6000 X-ray diffractometer) via Cu-Kα radiation (λ=0.154060 nm) at 40 kV. Fourier Transform Infrared Spectra (FTIR) was recorded with Perkin Elmer Spectrum 400 in the ATR mode via diamond ATR crystal in the wavenumber 4000–450 cm^{-1}. An Ocean Optics DH-2000 spectrophotometer recorded UV-visible spectra. EDX-equipped scanning electron microscope (SEM) was used to investigate the morphology (ZEISS Evo LS10). The polymer's specific surface area and pore characteristics were investigated with a Micromeritics Tristar II 3020 analyzer via N_2 adsorption-desorption isotherms at 77.3 K. The surface area and average pore diameter/pore volume of the polymer were calculated via Brunauer–Emmett–Teller (BET) and Barrett–Joyner–Halende (BJH) methods, respectively (Cryogenic Limited PPMS). The polymer's pH point of zero charges (pHpzc) was determined via a modified pH drift method [35, 36]. The electrical conductivity of the polymer was measured via a four-point probe electrical conductivity measurement method (ENTEK Electronics).

Table 1 Comparison of the photocatalytic performance of PDAAQ with other conductive polymer photocatalysts

Catalyst	Dye	Degradation efficiency, %	Degradation time (min)	Light source	References
PANI	MB	39	30	Visible light	[24]
	RdB	52	30		
PPy	RdB	48.18	45	Visible light	[20]
	DY	55.59	70		
Ppy/Fe	MG	95	60	UV light	[36]
PPy/CdS/Ni	MB	94.76	180	Visible light	[64]
PEDOT	MB	33.9	300	Visible light	[22]
TiO2/ZnO/PAN	MG	99	240	UV light	[65]
PTh/Al_2O_3	MB	77.3	240	Visible light	[66]
PDAAQ	MB	100	6	Visible light	This study
	DY	100	8		

PANI: polyaniline, PPy: polypyrrole, PEDOT: poly(3,4-ethylenedioxythiophene), PAN: polyacrylonitrile, PTh: polythiophene, RdB: rhodamine B, MG: malachite green

2.4 Dye Degradation Performance of PDAAQ

The adsorption-assisted photocatalytic activity of the PDAAQ polymer was assessed using an anionic azo dye DY and a hetero cationic polyaromatic dye MB. For adsorption studies, solutions were placed in the dark at room temperature, and dye solutions were removed at a predetermined moment, filtered, and measured using a UV-Vis spectrophotometer. Equations (1 and 2) can be used to determine the dye's adsorption capacity and the % removal, respectively [37, 38]:

$$qe = (C_0 - C_e) \times V/W \tag{1}$$

$$\text{Removal } (\%) = (C_0 - C_t) \times 100/C_0 \tag{2}$$

C_0 and C_e represent the starting and equilibrium concentrations of the adsorbed dye, respectively. C_t denotes the dye concentration at a certain place. The relative molecular weight of the dye is denoted by W (g/mol). V (L) represents the dye solution's volume.

Dye adsorption has traditionally been examined by the two important adsorption isotherms, the Langmuir equilibrium isotherm and the Freundlich equilibrium isotherm, as described in Eqs. (3 and 4) [39].

$$C_e/q_e = C_e/q_{max} + 1/(q_{max}K_L) \tag{3}$$

here, K_L represents the Langmuir constant, C_e represents the equilibrium concentration, and q_e and q_{max} denote the maximum and equilibrium adsorption capacities, respectively. C_e/q_e vs. C_e was plotted, and K_L and q_{max} values (Table 1) were computed by applying the slope and intercept of the linear curve derived from the Langmuir isotherm equation. Equation (4) contained the Freundlich isotherm equation.

$$\ln q_e = 1/n \ (\ln C_e) + \ln K_F \tag{4}$$

where q_e and C_e are the equilibrium adsorption quantity and concentration of the solutions, n is the degree of surface heterogeneity, and K_F is the Freundlich constant, representing the adsorption capacity. Equation 4 was used to plot $\ln q_e$ versus $\ln K_F$. The slope and interception of the linear curve obtained from the Freundlich isotherm equation were used to compute the 1/n and K_F values.

For the kinetic studies, pseudo-first and pseudo-second-order dye adsorption models were investigated. The pseudo-first-order model (Eq. 5) is the most employed approach to analyze the dye's dynamic adsorption performance,

examining the adsorption behavior at the liquid-solid interface to determine the adsorption rate [40]:

$$\mathrm{Ln}\ (q_e - q_t) = \ln q_e - k_1 t \quad (5)$$

here, q_t (mg/g) and q_e (mg/g) represent the quantity of dye adsorption at t time and equilibrium, respectively. k_1 represents the rate constant of pseudo-first-order adsorption. The pseudo-second-order model (Eq. 6) was also constructed, which is based on the notion that the adsorption capability is primarily related to the number of active sites occupied by the adsorbent [41]:

$$t/q_t = 1/k_2 qe^2 + t/q_e \quad (6)$$

here, k_2 is the rate constant of pseudo-second-order adsorption.

In adsorption-assisted photocatalysis experiments, the dye and photocatalyst were not expected to reach adsorption-desorption equilibrium, and the measured dye degradation amounts were called adsorption-assisted photocatalysis. Adsorption-assisted photocatalysis studies were carried out in the photoreactor. A halogen lamp was used as the light source in the photoreactor. During the experiments, UV-visible absorption spectra were recorded at two-minute intervals to monitor changes in the absorbance of the dye. From the absorption spectra recorded at different times during photocatalytic degradation, the % degradation values of the dyes were calculated according to Eq. (2), using the absorbance values measured at the wavelength at which they had maximum absorption in 650 and 390 nm for MB and DY, respectively [42].

Using pseudo-first and pseudo-second-order kinetic models, the kinetic behavior of the adsorption-assisted photocatalytic process in the simultaneous removal of DY and MB cationic dyes from aqueous solution was examined Eqs. (7 and 8) [43]:

$$-\ln\ (C_t/C_0) = k_1 \cdot t \quad (7)$$

$$1/C_t = 1/C_0 + k_2 t \quad (8)$$

here, the rate constants of the pseudo-first-order and pseudo-second-order kinetic models are C_0 (mg/L), which represents the concentration of dyes prior to the onset of the adsorption-assisted photocatalytic degradation process, and C_t (mg/L), which represents the concentration of dyes following the onset of the photocatalytic degradation process at times t (min), and k_1 (1/min), and k_2 (L/mol.min) are the rate constants of the adsorption- assisted photocatalytic process.

The performance of PDAAQ polymers synthesized using different solvents and oxidizing reagents in the photocatalytic removal of MB dye used as a model compound was also investigated. Due to their high photocatalytic dye degradation performance, it was decided to use ACN as the solvent and APS as the oxidant.

Stability experiments were performed using PDAAQ, at pH = 10.5 for MB and pH = 1 for DY, by conducting five experiments using the same photocatalyst and replacing the dye solutions between series to simulate an intensive industrial application. 1.2 mg of photocatalyst was dispersed into 3 mL of MB and DY solutions for the scavenging experiment. Then 0.1 M of ethylenediaminetetraacetic acid (EDTA), ascorbic acid ($C_6H_8O_6$), and isopropyl alcohol (IPA) were used as hydroxyl radical (·OH), singlet oxygen ($^1O_2$) and h^+ traps, respectively.

3 Results and Discussion

3.1 Structural Characterization

The structural characterization of PDAAQ was completed via FTIR, XRD, and UV-vis methods (Fig. 2). Figure 2a shows the FTIR spectrums of the DAAQ monomer and PDAAQ polymer. The characteristic absorption peaks of DAAQ at 3414, 3315, 1608, 1536, 1381, and 1264 cm^{-1} are attributed to -NH_2 asymmetric and symmetric vibrations, C = O (quinone), C-N-C stretching, and C = C stretching vibration of the anthraquinone ring, respectively [44]. After the polymerization was completed, the intensity absorption peaks of DAAQ were decreased and spread out. In the FTIR spectrum of PDAAQ, the absorption peak observed at 3348 cm^{-1} is due to the -NH_2 symmetric vibrations. The peak at 1602 cm^{-1} is attributed to C = O in the quinone ring. Also, the absorbance peaks C = C aromatic and C = N stretching is observed at 1580 and 129 cm^{-1}, respectively. The peaks at 1257 and 1172 cm^{-1} are due to the C-N stretching of the primary and secondary amine groups, respectively. Also, the peak at 1384 cm^{-1} is related to C-N-C stretching [44–46].

XRD analysis was conducted to investigate the crystal structure of the PDAAQ polymer. Figure 2b illustrates the typical XRD pattern of PDAAQ. The XRD pattern of the PDAAQ polymer shows low crystallinity. The broad peak centered at 25° can be related to periodicity and perpendicular to the polyaniline-like main chains [47, 48].

Figure 2c shows the UV-Vis absorption spectra of PDAAQ and DAAQ over the 200–1000 nm range. The spectrum of the DAAQ monomer exhibits a distinct absorption peak at 460 nm, whereas the PDAAQ polymer displays a broad and intense absorption spanning the entire range from 200 to 1000 nm, encompassing the UV, visible, and near-infrared

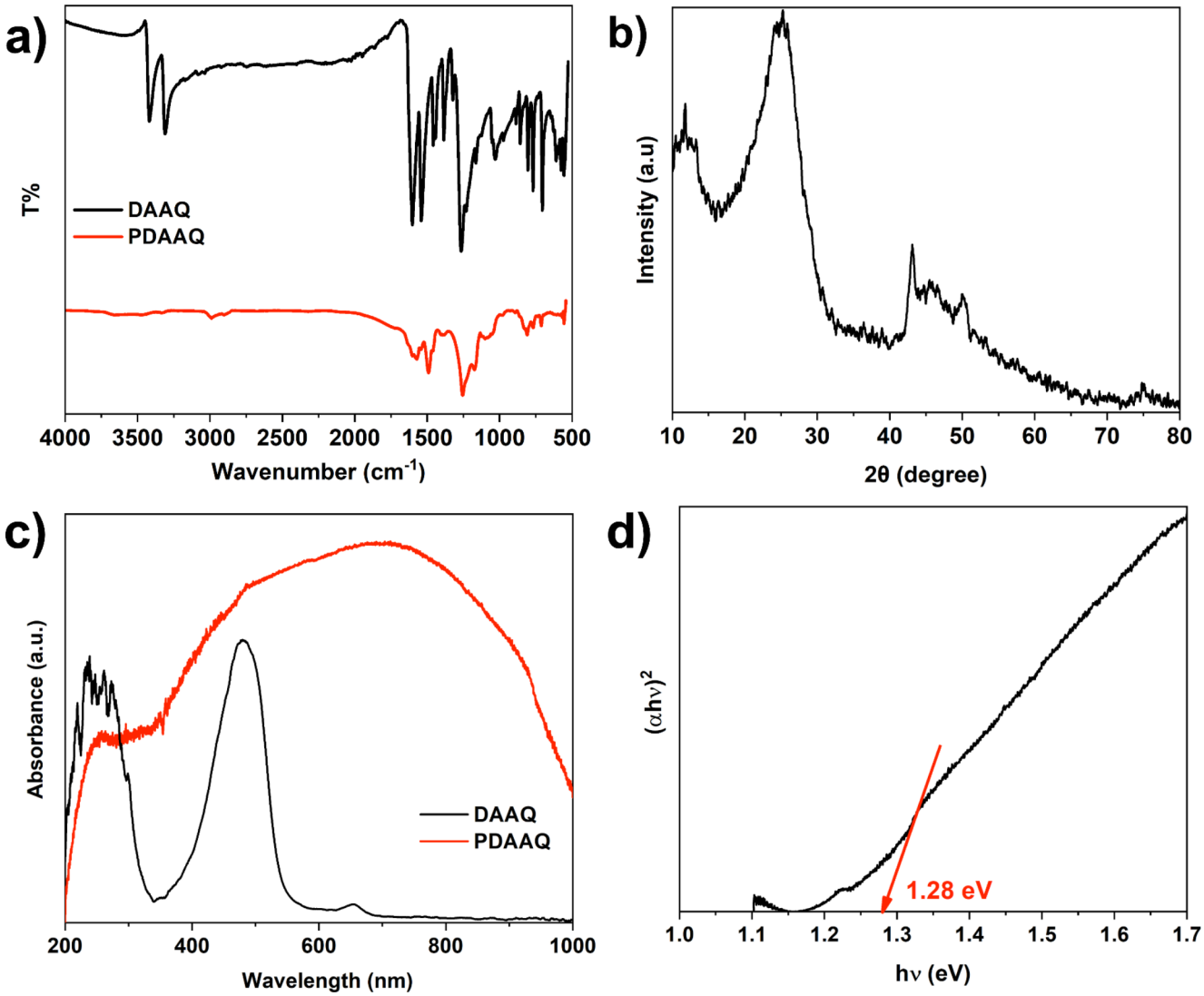

Fig. 2 **a** FTIR spectrums of DAAQ and PDAAQ, **b** XRD pattern, **c** UV-vis absorption spectrum, and **d** E_g estimation of PDAAQ (revised figure)

regions. The broad absorption band in the visible region is attributed to the π-conjugated system of PDAAQ [48]. The marked difference between the UV-Vis spectra of the monomer and the polymer indicates that the polymerization process extends conjugation and enhances electronic delocalization within the polymer structure, resulting in a significantly broadened and intensified absorption band compared to the monomer. Using the Tauc plot [13, 46], the optical energy band gap (Eg) of PDAAQ was determined from the absorption spectrum (Fig. 2d). The relationship $\alpha h\nu = A\,(h\nu - Eg)^2$ is used to calculate the material's optical band gap, where A, hν, and α are a constant, photon energy and the linear absorption coefficient, respectively. Plotting $(\alpha h\nu)^2$ as a function of hν allows for estimating the optical energy band gap of 1.28 eV.

3.2 Morphological Analysis

The SEM images depict distinct morphological structures of PDAAQ synthesized in various polymerization media. Images labeled with "i" reveal an overview of the surface morphology, while those labeled with "ii" provide a closer view, focusing on the yellow-framed regions in Figures a.i., bi, and ci. The morphological architectures of PDAAQ synthesized with various solvents change because of the impact of solvents on the polymerization process. Solvents are key in shaping polymer nucleation, growth, and self-assembly processes, directly impacting final morphology. Each solvent interacts differently with the monomers and growing polymer chains, influencing solubility, diffusion rates, and chain conformation. These interactions result in distinct microstructures observed in SEM images, such as particle size, shape, or surface texture variations. The morphological

structure is also one of the parameters affecting photocatalytic activity, and surface area and photocatalytic activity change depending on the morphological structure.

The PDAAQ polymer is successfully synthesized using an initiating system with chemical oxidative polymerization. Liu and Liu successfully synthesized PDAAQ polymer using an APS/$HClO_4$ oxidant/initiator system via chemical oxidative polymerization as supercapacitor electrode material [49]. Using the same oxidant/initiator couple, we synthesized PDAAQ via chemical oxidative polymerization in different polymer mediums: ethanol (EtOH), acetonitrile (ACN), and dichloromethane (DCM). The photocatalytic activities of polymers synthesized using EtOH, ACN, and DCM as solvents were investigated. Among these, the highest photocatalytic activity was observed for PDAAQ synthesized in ACN, leading to the selection of ACN as the optimal solvent for further studies. Furthermore, SEM imaging of the polymers synthesized in these three different solvents revealed distinct morphological differences (Fig. 3). These observations suggest that the choice of solvent not only influences the photocatalytic performance but also has a significant impact on the morphological characteristics of the resulting polymers. The superior performance of PDAAQ synthesized in ACN may be attributed to its morphology, which likely facilitates enhanced light absorption and improved interaction with reactants during photocatalysis.

PDAAQ was synthesized using ACN as a solvent and different oxidizing reagents as oxidants (APS, $K_2Cr_2O_7$, H_2O_2, $FeCl_3$), and SEM images of the synthesized polymers are shown in Fig. 4. Figure 4 shows the morphological structures of the polymers synthesized using different oxidants. The distinctive morphological structures of PDAAQ polymer synthesized using different oxidant types can be explained by the impact of oxidizing agents on the polymerization process. Oxidizing agents initiate and propagate the polymerization reaction and influence the growth kinetics, molecular weight, and aggregation behavior of the polymer chains, all of which contribute to the final morphology [50]. Different oxidizing agents have varying oxidation potentials and reactivity, which can lead to differences in the rate of polymer formation, chain propagation, and termination processes. These variations can influence the degree of polymerization, crystallinity, and the self-assembly of polymer chains. Consequently, the morphology observed in SEM images, such as changes in particle size, shape, or surface roughness, reflects these underlying polymerization dynamics. For instance, a more potent oxidizing agent might produce more branched or irregular structures, while a milder one could produce smoother or more compact structures. This diversity in morphology is significant because it can directly affect the polymer's properties, such as conductivity, surface area, and catalytic activity, which are often closely related to the material's microstructure.

The morphological analysis of PDAAQ synthesized at optimum conditions investigated the SEM, EDX mapping, and BET analysis (Fig. 5). The morphologies of PDAAQ were investigated using SEM observations. Figure 5a and b show the SEM of PDAAQ at different magnifications. Figure 5a shows the overall surface morphology of the PDAAQ polymer, representing a porous structure with a rough surface and aggregated particles. The image in Fig. 5b, a magnified portion highlighted in red Fig. 5a, provides a closer look at the individual agglomerates, suggesting the formation of nanoparticles or micro-sized particles. The elemental distribution of the PDAAQ polymer is analyzed using the EDX mapping method (Fig. 5c-f). The combined elemental map shows a uniform distribution of elements throughout the polymer matrix (Fig. 5c). The carbon (C-K) map indicates the carbon-based backbone of the polymer (Fig. 5d). Oxygen and nitrogen elements are also homogeneously distributed on the polymer surface (Fig. 5e, f). BET analysis was also performed to investigate the structural and porosity features of PDAAQ. The N_2 adsorption-desorption of PDAAQ was given in Fig. 5d. The PDAAQ polymer exhibits type IV isotherm due to the micro and mesoporous structure. Also, the pore size distribution of the PDAAQ polymer was determined by BJH analysis (inset Fig. 5d). The pore diameter, surface area, and pore volume of PDAAQ are 14.76 nm, 17.79 ∓ 0.8 m^2/g, and 0.065 cm^3/g.

Figure 6 shows the photoluminescence (PL) spectrum of the PDAAQ polymer, exhibiting a strong emission peak at approximately 600 nm wavelength. This peak reflects the $\pi \rightarrow \pi^*$ transitions of the polymer and its optical activity in the visible light region, confirming the photoluminescence properties of the material. The 200 nm Stokes shift calculated for the excitation wavelength of 400 nm indicates that electrons experience energy loss at intermediate energy levels and that the material may be affected by defects in energy transitions. The excitation wavelength of the PDAAQ polymer was selected as 400 nm, which might be associated with the $\pi \rightarrow \pi^*$ transitions of the aromatic units in the polymer structure. Side peaks and broad bands may be associated with defects in the polymer chain or environmental effects [51].

3.3 Electrical Conductivity

Using the four-probe method, the electrical conductivity of the PDAAQ pellet was measured as 1.23 S/cm at room temperature. PDAAQ's relatively low band gap is consistent with its modest electrical conductivity since smaller band gaps frequently facilitate electron migration from the valence band to the conduction band. This outcome is

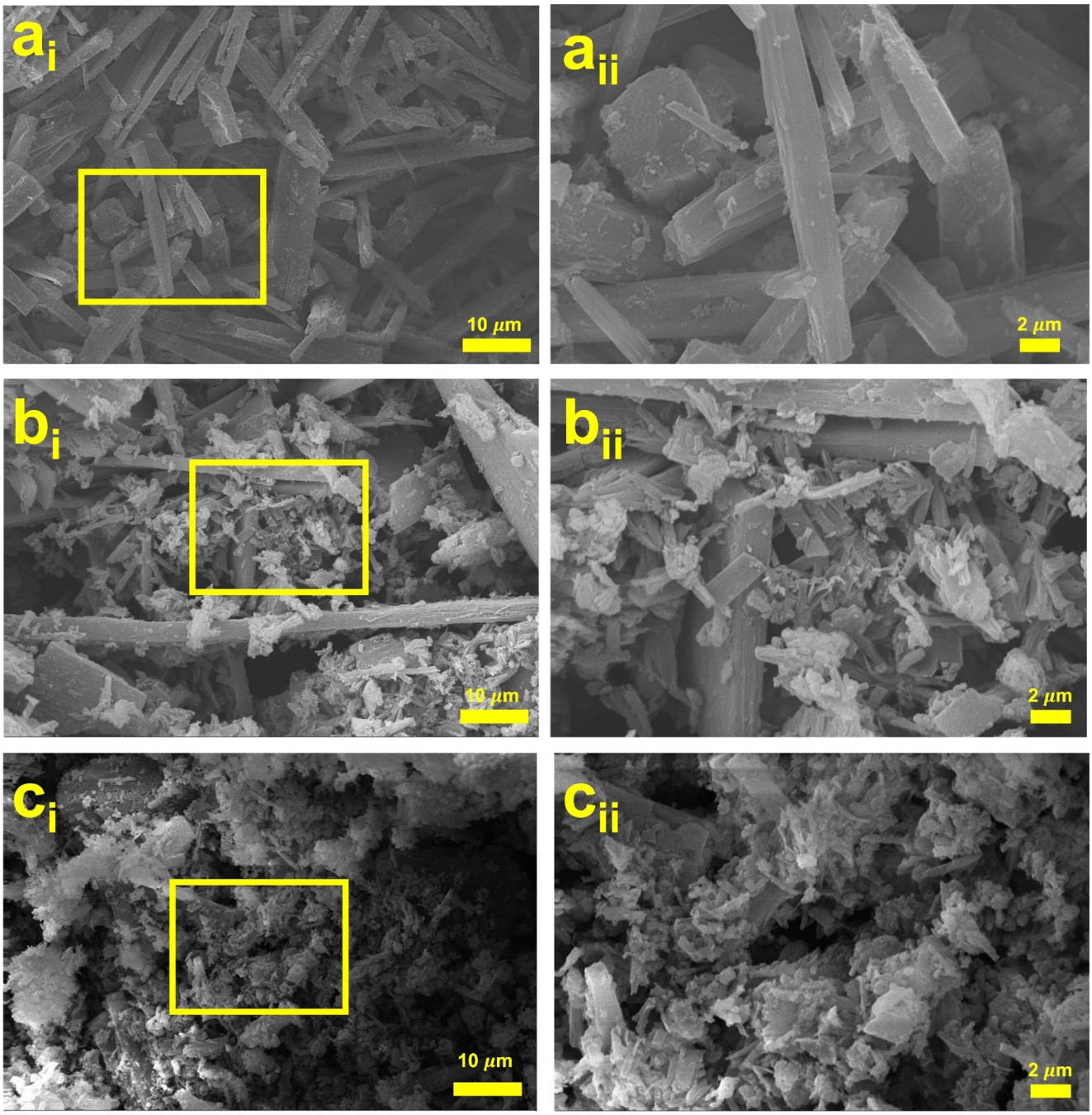

Fig. 3 SEM images of PDAAQ synthesized in **a** EtOH, **b** ACN, and **c** DCM medium (i and ii: images taken different magnifications)

similar to those of other conductive polymers with electrical conductivities ranging from 0.1 to 10 S/cm, such as polypyrrole (PPy) and polyaniline (PANI), depending on the synthesis parameters and degree of doping [52–54].

3.4 Dye Degradation Performance of PDAAQ

An evaluation of the photocatalytic performance of PDAAQ, synthesized with various solvents (ACN, DCM, and EtOH), in degrading MB dye as a model compound revealed that the polymers synthesized with ACN and DCM exhibited superior photocatalytic efficiency compared to the polymer produced with EtOH (Fig. 7a). However, in the case of the DCM used as the solvent, the synthesized polymer's synthesis yield was lower than that of the polymer synthesized in the ACN medium. The lower polymerization yield in DCM is attributed to the limited solubility of the monomer and the oxidant during the polymerization

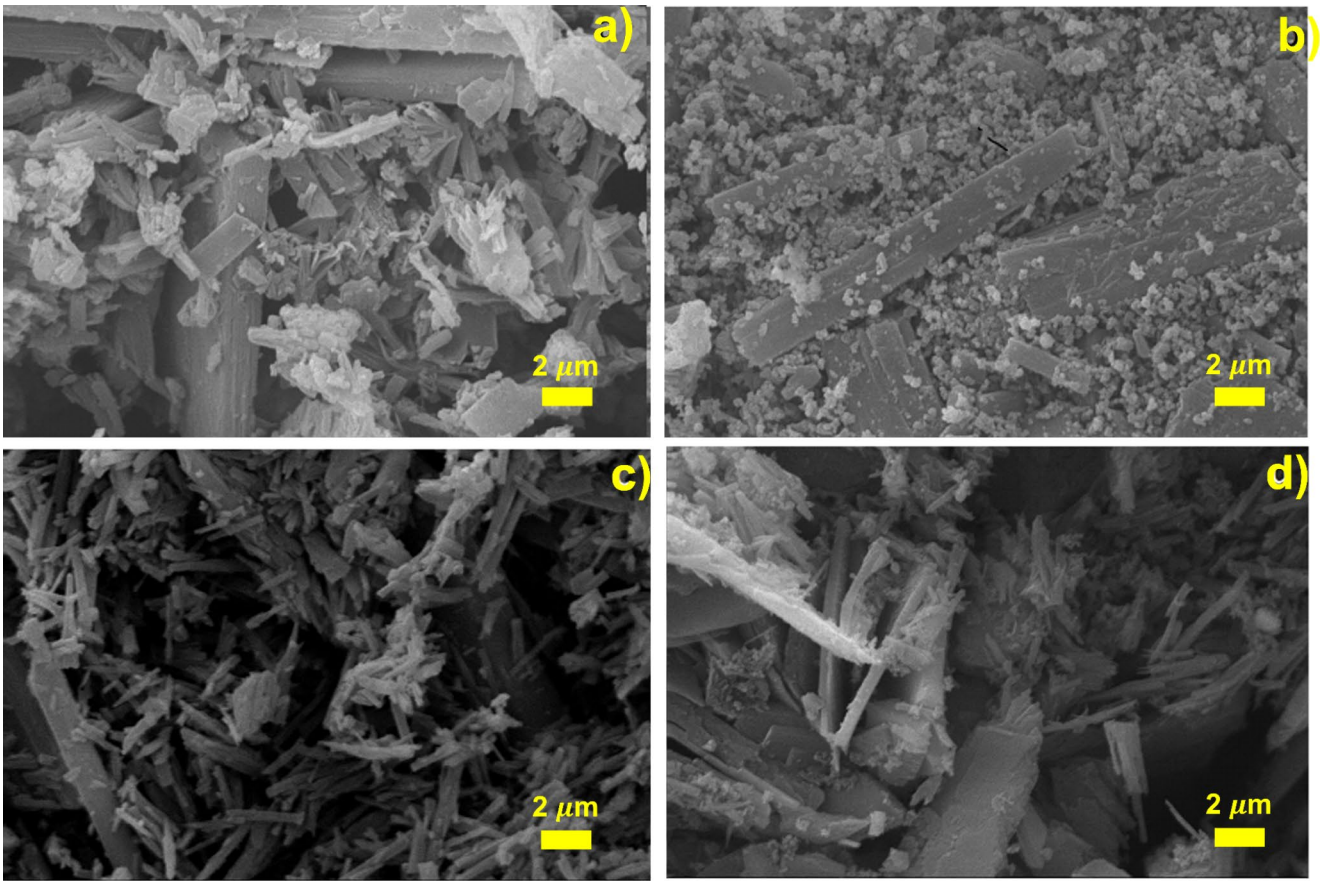

Fig. 4 SEM images of PDAAQ synthesized by using **a** APS, **b** $K_2Cr_2O_7$, **c** H_2O_2, **d** $FeCl_3$ as an oxidant

process, reducing the reaction rate or leading to incomplete polymerization and resulting in lower yield. Solvent polarity is another critical factor in chemical polymerization, as it affects the solubility of reactants and the mobility of growing polymer chains. DCM's relatively low polarity may not support the efficient propagation of polymer chains, leading to lower yield. Solvents act as a medium for the chemical polymerization reaction and influence the polymer's molecular structure, morphology, and surface properties, which are crucial for photocatalytic activity. The effect of the solvent on the polymerization process and the final polymer structure explains the increased photocatalytic activity of PDAAQ generated with ACN as a solvent as opposed to that synthesized in ethanol. Because ACN is a moderately polar aprotic solvent, it facilitates more effective polymerization, which probably produces a polymer with a higher degree of conjugation. In conductive polymers like PDAAQ, conjugation is essential for facilitating charge separation and transfer, processes that are critical for photocatalytic activity. The increased conjugation improves electron mobility within the polymer, enhancing its ability to generate reactive species under light and degrading MB at higher rates. ACN may also promote the development of a polymer structure with a higher surface area and greater porosity, which would increase the number of active sites available for dye adsorption and degradation. Ethanol, a polar protic solvent, may lead to a polymer with a lower degree of conjugation and less ordered structure due to its hydrogen bonding and polarity, which can interfere with the polymerization process. The reduced conjugation decreases the polymer's capacity for efficient charge transfer, directly limiting its photocatalytic performance. Additionally, the polymer synthesized in ethanol may exhibit less favorable surface properties, such as lower porosity or fewer active sites for MB dye adsorption, further contributing to the lower photocatalytic activity. In conclusion, the solvent choice significantly affects the polymer's electronic properties and morphology, with ACN leading to a more efficient photocatalytic material than ethanol. On the other hand, being a polar protic solvent, ethanol may affect the polymerization process differently. It may inhibit the production of prolonged conjugated chains or result in a less ordered or porous polymer structure, reducing conjugation and surface area and thus limiting the polymer's capacity to create and transmit charge carriers, resulting in poorer photocatalytic effectiveness. Ethanol may interact with the polymer during

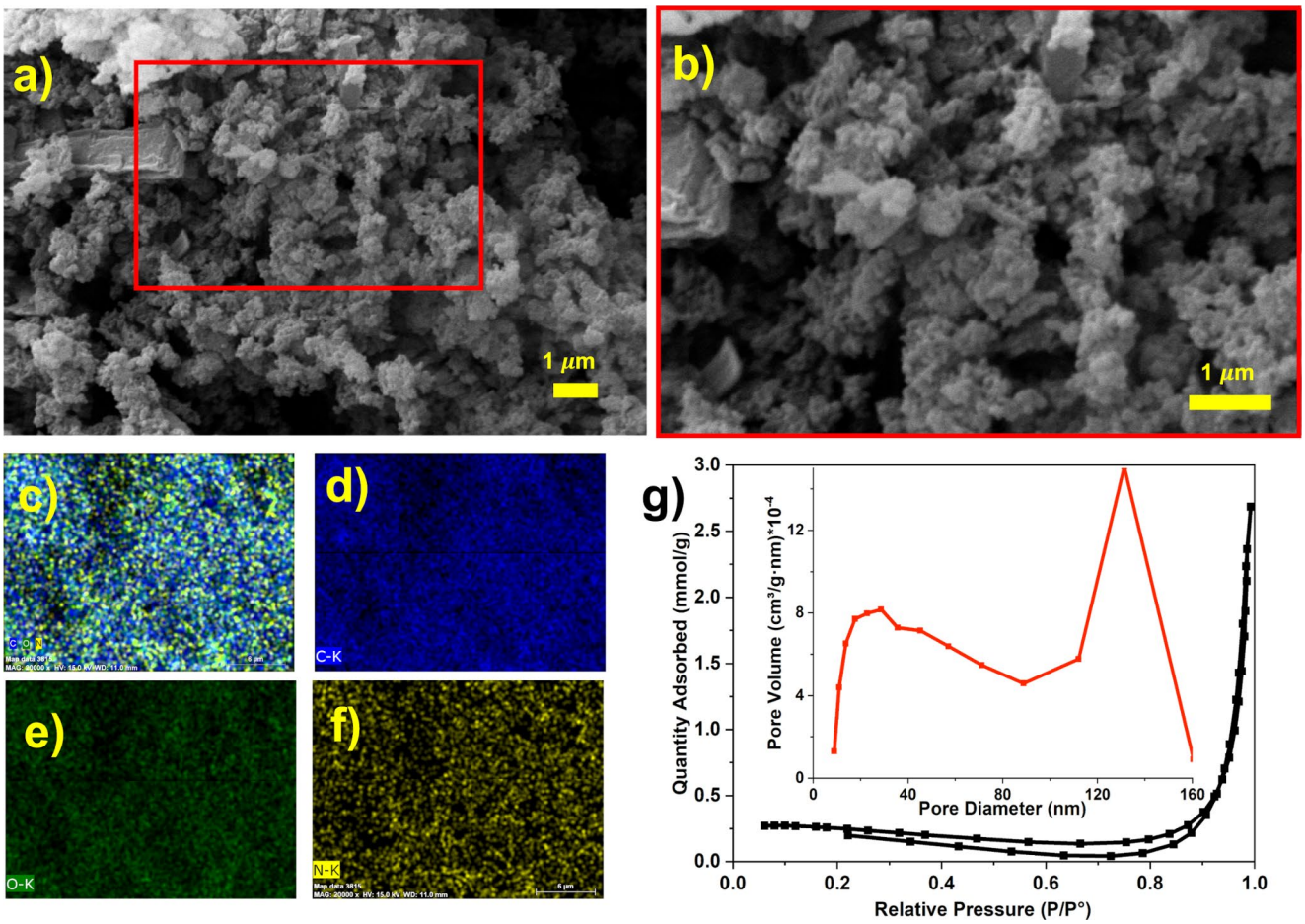

Fig. 5 **a**, **b** SEM images of PDAAQ synthesized using ACN as the solvent and APS as the oxidant, **c**–**f** EDX mapping of C, O, and N elements, **g** N_2 adsorption-desorption isotherms and inset BJH pore size dispersion plots of PDAAQ

manufacture, limiting the availability of active sites and decreasing the degradation efficiency of the MB dye. Thus, the choice of solvent strongly impacts the shape and electrical characteristics of the produced PDAAQ, which then affects its photocatalytic efficacy [55].

The oxidant type significantly impacts the photocatalytic dye degradation performance of PDAAQ under visible light. The oxidants employed to manufacture the PDAAQ were $FeCl_3$, APS, H_2O_2, and K_2CrO_7. The maximum photocatalytic performance was observed in the presence of PDAAQ and APS as an oxidant (Fig. 7b). APS acts as an oxidizing agent that begins the polymerization reaction, and its concentration is critical in defining the polymer chain length, molecular weight, and overall shape of the polymer, which impacts its photocatalytic efficacy [56, 57].

Polymerization time is another critical factor affecting the photocatalytic dye degradation performance of PDAAQ. Figure 7c shows the photocatalytic dye degradation performance of PDAAQ polymer synthesized at different polymerization times in degradation MB dye under visible light. As polymerization time increases, crystallinity and structural stability increase. However, as the polymerization time increases, the polymer chains overlap, causing a decrease in surface area and, thus, decreasing the photocatalytic active sites. According to Fig. 6c, the optimum synthesis time was decided as one hour.

The PDAAQ produced with a 1:3 monomer-to-oxidant (APS) ratio showed better photocatalytic activity in the degradation of MB dye, which may be ascribed to the impact of oxidant concentration on the polymer structure and characteristics (Fig. 7d). At a 1:3 monomer-to-oxidant ratio, the higher APS concentration may lead to more effective oxidation, resulting in better crosslinking and a higher degree of conjugation in the polymer. This enhanced conjugation improves the electron mobility within the polymer, facilitating more efficient charge separation and transfer during photocatalysis. Furthermore, a higher oxidant concentration affects the resultant polymer's surface area and porosity, which are important for dye adsorption and subsequent photocatalytic destruction. The increased surface area affords more active sites for interaction with MB molecules, resulting in higher photocatalytic activity. In contrast, the

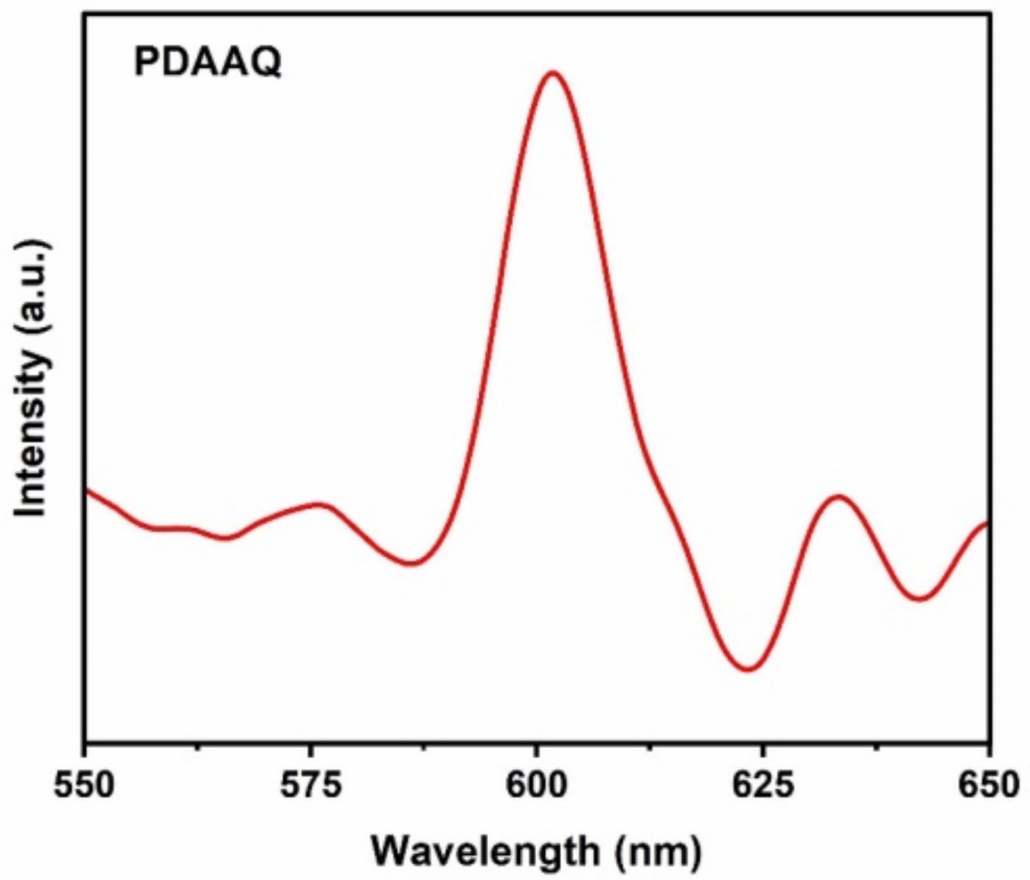

Fig. 6 Photoluminescence spectra of PDAAQ

polymer may have less crosslinking and a lower degree of conjugation at lower oxidant ratios, restricting its capacity to produce and transfer charge carriers effectively and diminishing the photocatalytic efficacy. This result suggests that optimizing the monomer-to-oxidant ratio is critical to enhancing the polymer's photocatalytic properties [55].

The pH drift technique was used to obtain the pH PZC [36, 56]. Particularly in aqueous environments, pH is essential to the photodegradation of organic molecules [58]. Reactive species generation and other modifications to catalyst surface characteristics are pH-dependent and impact catalyst efficiency [59]. The pHpzc plot of the PDAAQ is shown in Fig. 8a, and the estimated value of 2.82 is found at the intersection of the final pH line and the beginning pH. The surface will be positively charged at pH values lower than 2.8 because the acidic environment causes surface functional groups, including hydroxyl groups, to protonate and acquire protons (H^+). However, as the pH increases beyond 2.8, these groups deprotonate, losing hydrogen ions, which results in a negatively charged surface [58].

The effects of pH, catalyst dosage, and dye concentration were examined to comprehend how operational circumstances affected the photodegradation of the dyes under visible light. The photocatalysis efficiency of PDAAQ was investigated under dark and visible light irradiations in the existence of MB and DY dyes. The photocatalytic efficiency of the catalyst is known to be determined by the pH of the reaction medium. The photocatalytic performance of the generated PDAAQ was tested against the shifting pH of the MB and DY solutions, which ranged between 1 and 10.5 (Fig. 8b). The solution's pH was adjusted using H_2SO_4 and NaOH. MB dye removal efficiencies increased at pH values of 5, 6, 7, 9, and 10.5, all higher than the pH PZC (2.82). At these pH values, the surface of PDAAQ is deprotonated with a negatively charged surface, increasing the photocatalytic efficiency of PDAAQ when exposed to visible light, and MB dye is completely degraded [60]. DY dye removal

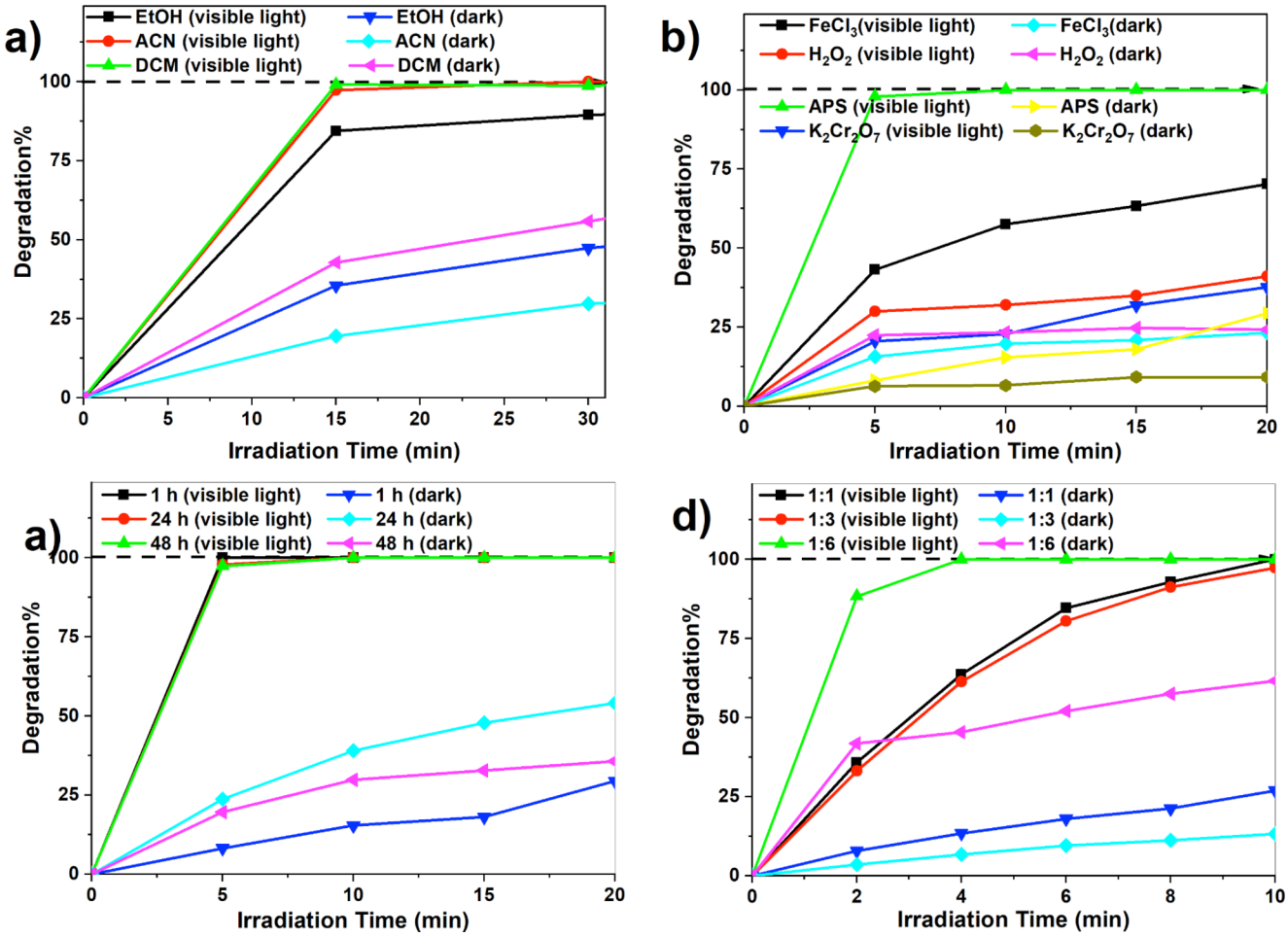

Fig. 7 The effect of **a** polymerization medium, **b** oxidant type, **c** polymerization time, and **d** monomer: oxidant ratio on the degradation of MB under dark and visible light illumination (dye concentration: 10 µM and photocatalyst dosage: 1.3 mg/mL)

efficiencies were greater for pH values of 1, 2, and 3, which are lower than the pHpzc. At pH 1, the maximal degradation for DY was achieved. The surface of PDAAQ has a positive charge at this pH, and DY takes on a zwitterionic shape in a polar solvent. Thus, the catalyst surface and the DY dye molecule attract one another. At low pH, the positive holes are the main oxidizing species [20]. Since the PDAAQ structure's amino groups may be protonated with more protons at lower pH values, the structure's positive charge density will increase [32]. The dye removal rate increases because of the strong electrostatic contact between the PDAAQ surface and the dye anions, and the removal efficiency decreases as the pH rises. These electrostatic interactions between the dye molecules and the PDAAQ surface thus caused the differences in dye removal at various pH levels.

Using PDAAQ with a fixed MB concentration of 10 µM and a pH of 1, the effects of adsorption and adsorption-assisted photocatalysis on MB removal were studied with the photocatalyst amount ranging from 0.1 to 1.3 mg/mL. Increasing the dosage of PDAAQ resulted in higher adsorption capability (Fig. 8c). At 1.3 mg/mL PDAAQ, the highest adsorption rate (82%) was achieved. The increase in surface area leads to more active adsorption sites [61]. With adsorption-assisted photocatalysis, the percentage removal of MB dye gradually increased as the PDAAQ photocatalyst dosage increased attributed to more active sites with higher catalyst concentrations. Using 1.3 mg/mL of catalyst resulted in 100% decolorization efficiency. As a result, 1.3 mg/mL was chosen as the optimal catalyst dose. Photocatalyst dosages of 0.1 to 1.3 mg/mL were examined for their impact on DY degradation at a dye solution concentration of 10 µM and a pH of 1. Similarly, for DY dye, the adsorption amount increased to 52% by increasing the amount of photocatalyst from 0.1 to 1.3 mg/mL (Fig. 8d). In the adsorption-assisted photocatalysis of DY dye in the presence of PDAAQ photocatalyst, photodegradation reached 100% when the photocatalyst dosage was 0.4 mg/L. However, a further increase in photocatalyst dosage led to a slight decrease in DY degradation to 95%. Higher catalyst loading leads to increased photodegradation as it accelerates

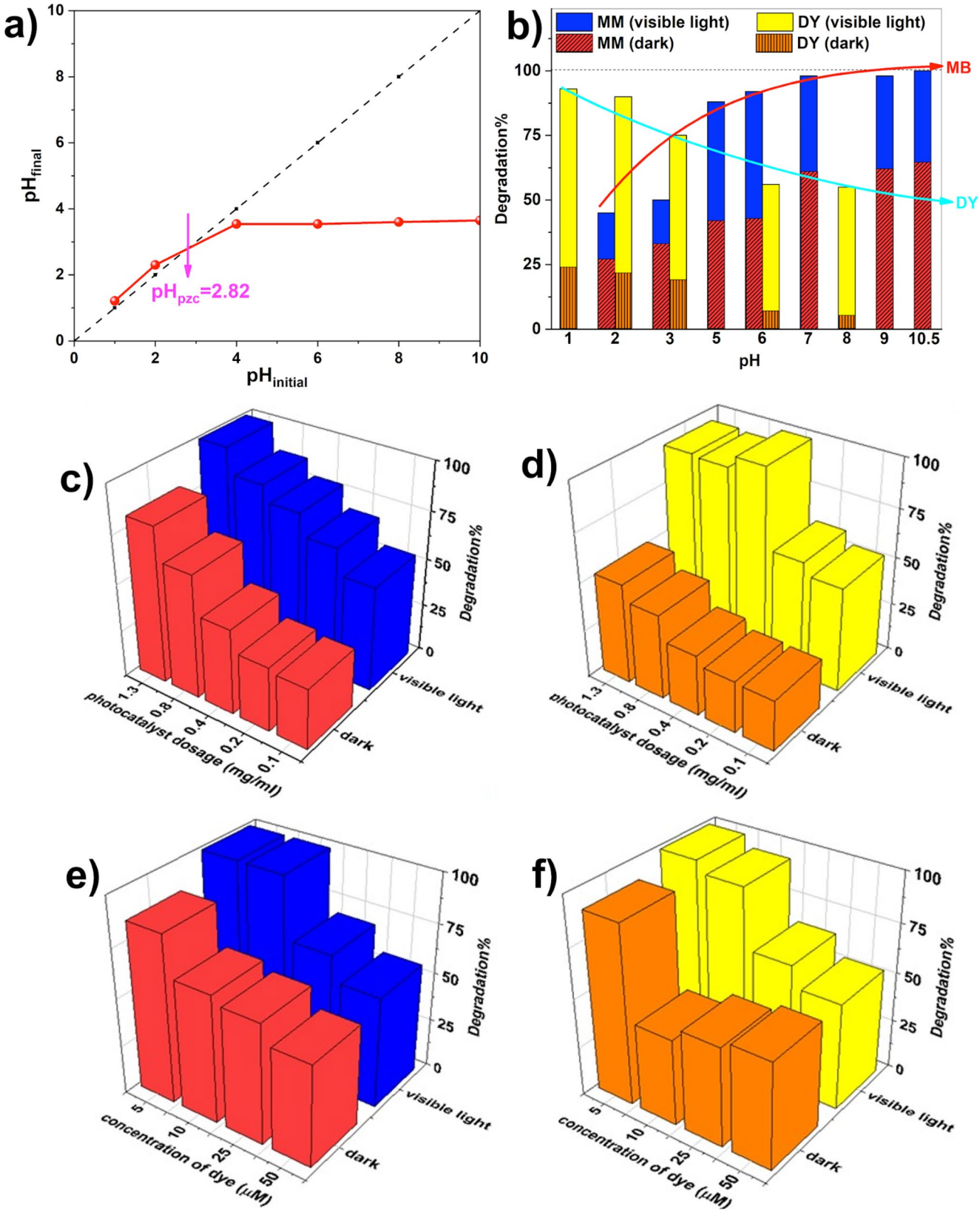

Fig. 8 **a** pHpzc of PDAAQ, the effect of **b** dye pH (dye concentration: 10 μM and dosage: 0.4 mg/mL), photocatalyst dosage on **c** MB (dye concentration: 10 μM and irradiation time: 2 min) and **d** DY (dye concentration: 10 μM and irradiation time: 8 min) and dye concentration of **e** MB (catalyst dosage: 0.4 mg/mL and irradiation time: 6 min) and **f** DY (catalyst dosage: 0.2 mg/mL and irradiation time: 10 min) under dark and visible light illumination

the formation of electron-hole pairs and hence ·OH radicals. However, because the suspended particles protect light, too much catalyst reduces light penetration, which lowers photodegradation [60].

The impact of dye concentrations (5, 10, 25, and 50 µM) on MB photodegradation is illustrated in Fig. 8e. According to the figure, it is obtained that as the dye concentration increases, adsorption decreases. The primary explanation might be the saturation of accessible adsorption sites on the material's surface. There are many free sites for dye molecules to adsorb at low concentrations, resulting in high adsorption efficiency. However, when concentration increases, the active sites are filled, resulting in an adsorption plateau [62]. The degradation percentage of MB at 5 µM and 10 µM was 100%, while it was found to be 69.82 and 56.82% at 25 µM and 50 µM, respectively. The degradation efficiency remained constant while increasing the dye concentration from 5 to 10 µM MB. On the other hand, the MB degradation on photocatalyst reduced considerably at dye concentrations of 25 µM and 50 µM. At low dye concentrations, only a small amount of dye is adsorbed onto the catalyst surface, and as the concentration of dye increases, the number of adsorbed dye molecules decreases the amount of light interacting with the catalyst surface needed to form an electron-hole pair. At higher dye concentrations, however, the number of photons reaching the catalyst surface decreases as more light is absorbed by the dye molecules, lowering the final catalyst efficiency [63]. This situation is like the degradation of DY dye on the PDAAQ photocatalyst surface shown in Fig. 8f. The PDAAQ polymer exhibits high degradation efficiency at 5 µM (90.65%) in DY dye adsorption, followed by a reduction at 10 µM (43.83%). The catalyst's active sites being saturated, which restricts the adsorption capacity as the dye concentration rises, is probably the cause of this decline. Nevertheless, an increasing trend in degrading efficiency is observed when the concentration rises from 10 to 50 µM, where the efficiency increases from 50.48 to 54.1%, respectively. The dye molecules may be able to occupy new or less accessible active sites due to enhanced mass transfer effects and possible secondary interactions. Furthermore, the adsorption kinetics may be changed by dye aggregation at greater concentrations, which might explain this apparent increase in degradation [61].

The reuse of catalysts is crucial for industrial applications. To evaluate their performance, PDAAQs were subjected to five consecutive experiments involving both MB and DY dyes. As illustrated in Fig. 9a, b and a consistent decline in the degradation efficiency of PDAAQ was observed across both dyes with repeated catalyst use. In Fig. 9a, the removal of MB by the PDAAQ photocatalyst after the first run reached 100% in 6 min, and the percentage color removals after 6 min were 81.39, 81.67, 78.06, and 71.43% for the 2nd, 3rd, 4th and 5th uses, respectively. The times required for 100% degradation of MB by the PDAAQ photocatalyst are 12, 14, 16, and 16 min for the 2nd, 3rd, 4th, and 5th uses, respectively. In Fig. 9b, the removal of DY with PDAAQ photocatalyst reached 100% at the end of 8 min after the first run. At the end of 6 min, the color removal percentages in the 2nd, 3rd, 4th, and 5th uses were 93, 89.5, 87.4, and 86.01%, respectively.

Table 1 compares the photocatalytic performance of the synthesized PDAAQ polymer with the other conductive polymer photocatalysts [20, 22, 24, 36, 64–66]. The PDAAQ photocatalyst requires comparatively shorter degradation times for degradation model dyes visible light irradiation.

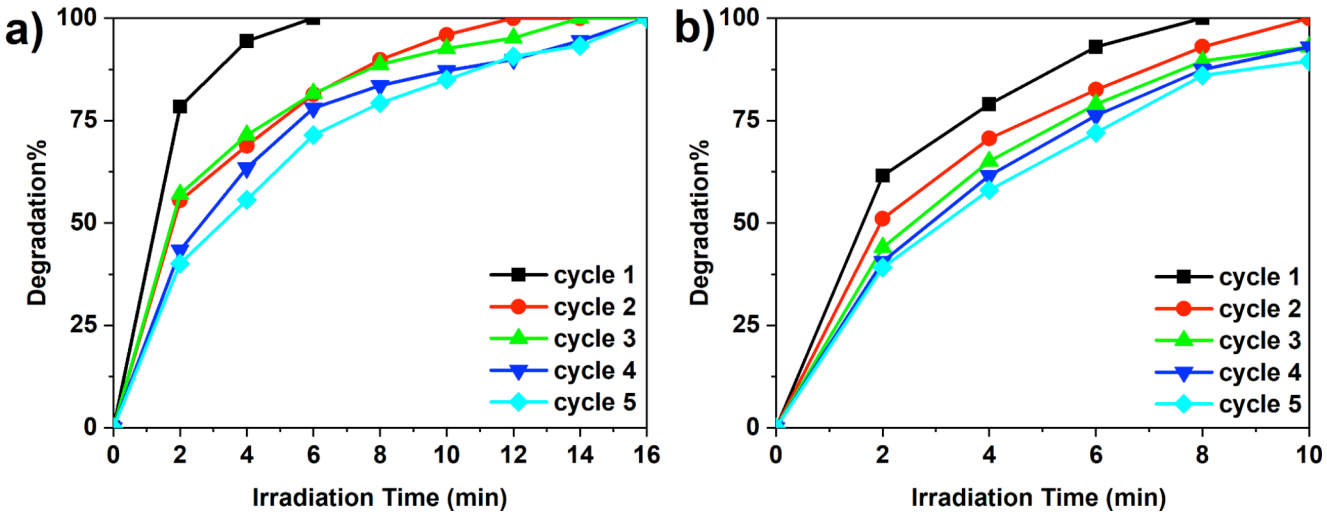

Fig. 9 The photocatalytic stability of PDAAQ (**a**) MB and (**b**) DY (dye concentration:10 µM, photocatalyst dosage: 0.4 mg/mL)

3.5 Photocatalytic Dye Degradation Mechanism

The photogenerated active species hole (h^+), superoxide anion ($\cdot O_2^-$), and hydroxyl ($\cdot OH^-$) radicals play crucial roles in the photocatalytic degradation process. Trapping experiments utilizing various scavengers were performed to investigate a possible photocatalytic mechanism. EDTA, isopropyl alcohol (IPA), and ascorbic acid (AA) functioned as scavengers to capture h^+, $\cdot OH^-$, and $\cdot O_2^-$ radicals [67]. The results of the experimental trapping are presented in Fig. 10a. The degradation efficiency of dyes is markedly reduced in the presence of AA. Moreover, the degradation efficiency is also affected by the inclusion of EDTA and IPA. In the photocatalytic degradation of dyes in the presence of PDAAQ under visible light, $\cdot O_2^-$ serves as the primary reactive radicals, while h^+ and $\cdot OH$ act as secondary reactive species.

The results from the scavenger experiments contributed to the demonstration of the proposed possible photocatalytic dye degradation mechanism of PDAAQ in Fig. 10b. The Eg value was estimated to be 1.28 eV (Fig. 2d). The cyclic voltammogram (CV) of PDAAQ was recorded in ACN+$LiClO_4$ medium within the voltage range of −0.5 to +2.0 V (Fig. S1). The initial oxidation potential (E_{ox}) of PDAAQ was determined to be 0.88 V from CV. The calculations for the highest occupied molecular orbital (HOMO) and lowest unoccupied molecular orbital (LUMO) of the PDAAQ are performed using Eqs. (9–11). The absolute vacuum scale (AVS) needs conversion to a normal hydrogen electrode (NHE) for further studies on photodegradation mechanisms. The calculated energy levels for HOMO and LUMO are 0.79 eV and −0.49 eV (relative to NHE), respectively.

$$E_{HOMO} = -\left(E_{(ox)} - E_{Fc} + 4.8\right)\ eV \tag{9}$$

$$E_{HOMO} = E_{LUMO} - E_g \tag{10}$$

$$E_{NHE} = -E_{AVS} - 4.5 \tag{11}$$

The PDAAQ polymer immediately adsorbs MB and DY through hydrogen bonding, van der Waals forces, π–π interactions, and electrostatic interactions [68] Subsequently, the electrons (e^-) and holes (h^+) are produced by exposure to visible light [69]. The hierarchical π–π arrangement in the PDAAQ polymer chain facilitates the separation and transfer of e^- and h^+ [50]. The LUMO level potential of the PDAAQ polymer is lower than the reduction potential of $O_2/\cdot O_2^-$ (−0.33 eV versus NHE) [70]; thus, electrons can generate $\cdot O_2^-$ with O_2 dissolved in water [63]. Nevertheless, the photogenerated holes of the PDAAQ were incapable of oxidizing OH^- to $^{\cdot}OH$, as the HOMO level potential was insufficiently positive (0.49 V). Consequently, the $^{\cdot}OH$ generated in the system originated from $O_2^{\cdot -}$ according to Eqs. (12 and 13) [68, 71].

$$O_2^{\cdot -} + H_2O \rightarrow {}^{\cdot}OOH + OH^- \tag{12}$$

$$H_2O + {}^{\cdot}OOH + e- \rightarrow {}^{\cdot}OH + OH^- \tag{13}$$

Simultaneously, h^+ can directly engage in the photodegradation of MB and DY. Dyes are effectively degraded

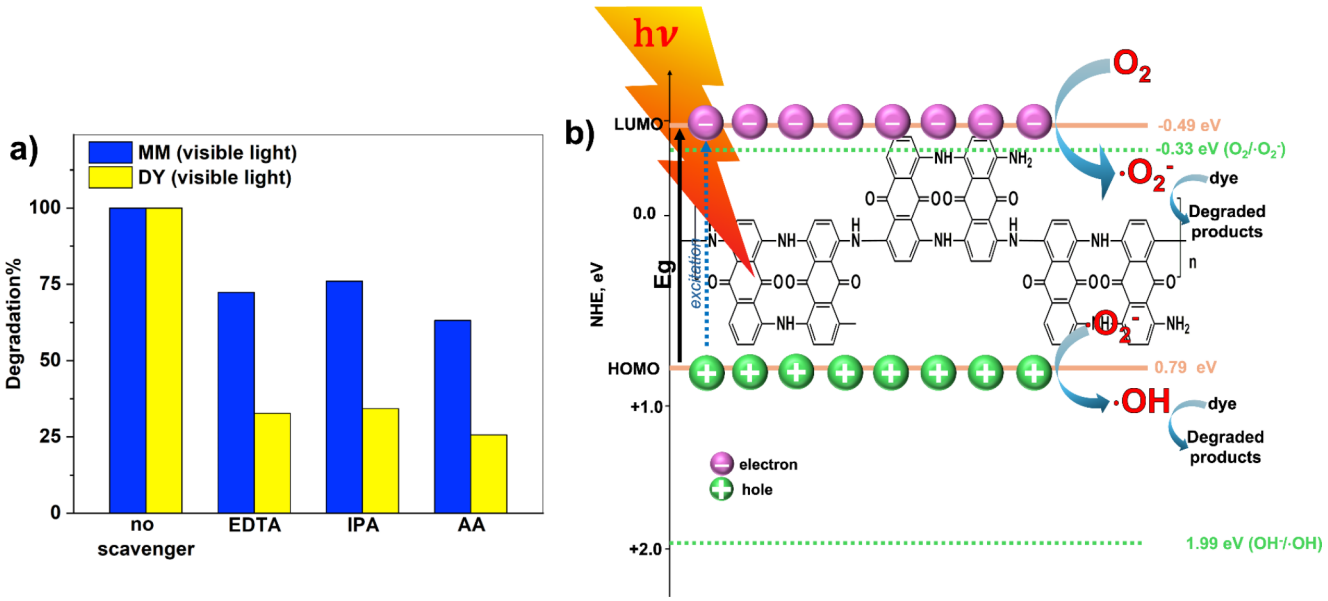

Fig. 10 **a** Scavenging experiment of active species during photocatalytic degradation of MB, DY dyes **b** proposed possible photocatalytic dye degradation mechanism

via the mechanism of adsorption-assisted photocatalytic degradation.

3.6 Adsorption Studies of PDAAQ

To understand the mechanics of the adsorption process, one must understand how dye molecules interact with the adsorbent surface and how long it takes for equilibrium to be attained. Figure 11a displays the plot of the dyes' equilibrium concentration (Ce) in the solution against the amount of dyes adsorbed (qe). The nature and adsorption capability of MB and DY dye molecules on PDAAQ were examined using Langmuir and Freundlich isotherm models. Figure 10b and c show the linear graph of C_e/q_e against Ce using Eq. (3) and $\ln C_e$ against $\ln q_e$ using Eq. (4).

As seen in Fig. 11b and c, the R^2 value for the Langmuir isotherm scenario of PDAAQ elimination on both MB and DY dyes was determined to be greater than the value determined for the Freundlich model.

The Freundlich isotherm suggests heterogeneous adsorption on a surface with different affinities. On the other hand, the Langmuir isotherm indicates monolayer adsorption on a surface with a small number of identical sites, indicating that MB molecules engage aggressively with the PDDAQ surface to cause saturation at greater concentrations [71, 72]. Table 2 shows the constants obtained from the Freundlich and Langmuir isotherms.

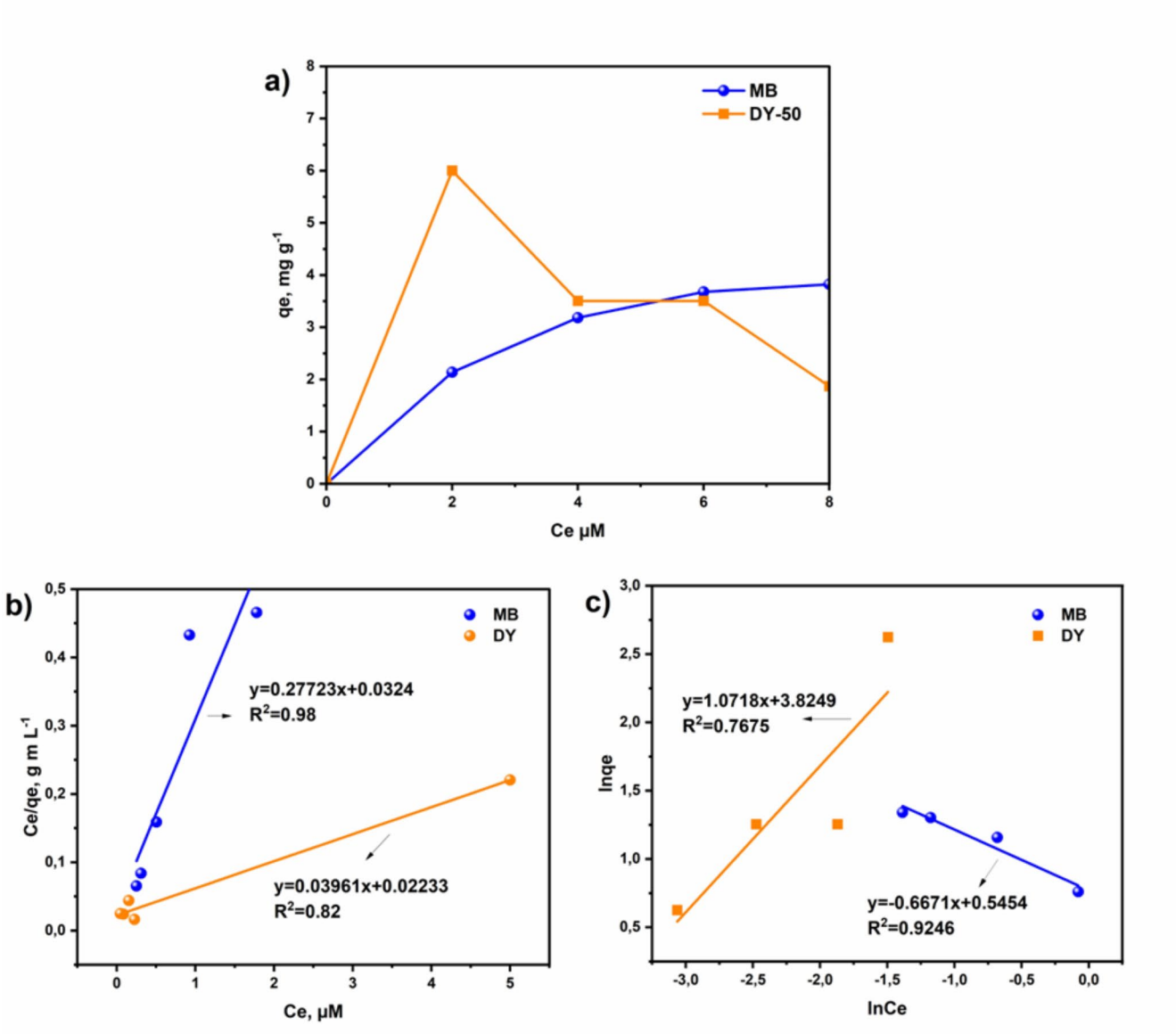

Fig. 11 **a** Change in the quantity of dye adsorbed at equilibrium (q_e) in relation to the dye's equilibrium concentration (C_e) plot, **b** Langmuir isotherm model and **c** Freundlich isotherm model for MB and DY dyes

Table 2 Langmuir and Freundlich isotherm constants and Linear (R^2) regression coefficient

MB		DY	
Langmuir	Freundlich	Langmuir	Freundlich
q_{max}= 3.6 mg g^{-1}	K_F= 1.72 mg g^{-1}	q_{max} = 25.24 mg g^{-1}	K_F= 45.82 mg g^{-1}
K_L= 111.1 L g^{-1}	1/*n*= −0.67 L g^{-1}	K_L= 1.77 L g^{-1}	1/*n*= 1.07 L g^{-1}
R^2=0.98	R^2=0.92	R^2=0.82	R^2=0.77

Table 3 Kinetics parameters

MB		DY	
Pseudo-first order	Pseudo-second order	Pseudo-first order	Pseudo-second order
k_1=1.24 min^{-1}	k_2=0.07 g mg^{-1} min^{-1}	k_1=0.92 min^{-1}	k_2=0.014 g mg^{-1} min^{-1}
q_e=4.43 mg g^{-1}	q_e=5.2 mg g^{-1}	q_e= 22.2 mg g^{-1}	q_e= 29.37 mg g^{-1}
R^2=0,98	R^2=0,99	R^2=0,99	R^2=0,99

The K_L of 111.1 L/g and the $_{max}$ of 3.6 mg/g in the Langmuir isotherm study for MB indicate a very high affinity of PDAAQ for MB, showing effective monolayer adsorption despite limited capacity [73]. A more significant amount of dye may be adsorbed but with less binding strength, according to DY, whose higher $_{max}$ of 25.24 mg/g and lower K_L of 1.77 L/g indicate better adsorption capacity with weaker affinity compared to MB [74]. The negative n_1 value (−0.67) in the Freundlich isotherm data suggests non-favorable or inconsistent adsorption, indicating that MB adsorption does not fit well [75]. On the other hand, DY exhibits favorable and multilayer adsorption with a positive n_1 value of 1.07. This disparity is further demonstrated by the K_F values, which show that DY has a substantially greater adsorption capacity than MB [76]. These findings imply that PDAAQ is more effective in adsorbing DY than MB.

Kinetic studies were conducted to examine dye adsorption behavior. The adsorption process's controlling kinetic mechanism was assessed using pseudo-first and pseudo-second order equations. Figure 12 shows the pseudo-first and pseudo-second order graphs of MB and DY dyes.

When Fig. 12 is examined, it is seen that both dyes obey pseudo-second-order kinetics, suggesting that chemical interactions between the dye molecules and the polymer surface's active sites constitute the rate-limiting process [39]. This trend implies that rather than being controlled by the concentration gradient, the creation of chemical bonds or interactions mainly drives the adsorption process. According to the pseudo-second-order model, the number of sites and the adsorbate concentration determine the adsorption rate, leading to a slow approach to equilibrium as the sites get saturated. This behavior is explained by the strong hydrogen bonding and electrostatic interactions between the dye molecules and the functional groups found in the PDDAQ polymer [77]. Table 3 displays the values of k_1, $q_{e,}$ and R^2 as calculated by Eqs. 5 and 6.

Table 3 shows that the theoretical adsorption capacity (q_e) for MB was 4.43 mg/g, and the first-order rate constant (k_1) was 1.24 min^{-1}. The second-order rate constant (k_2) was marginally higher at 0.07 g× $mg^{-1}min^{-1,}$ and q_e was 5.2 mg/g. The higher q_e value in these data suggests a chemisorption-dominated absorption process, and the second-order kinetics yielded a better match [78]. A better fit for the second-order kinetics is suggested by the fact that the first-order k1 for DY was 0.92 min^{-1} with a q_e of 22.2 mg/g, while the second-order k_2 was 0.014 g× $mg^{-1}min^{-1}$ with a q_e of 29.37 mg/g. The adsorption process appears slower but more persistent because of the higher q_e and lower

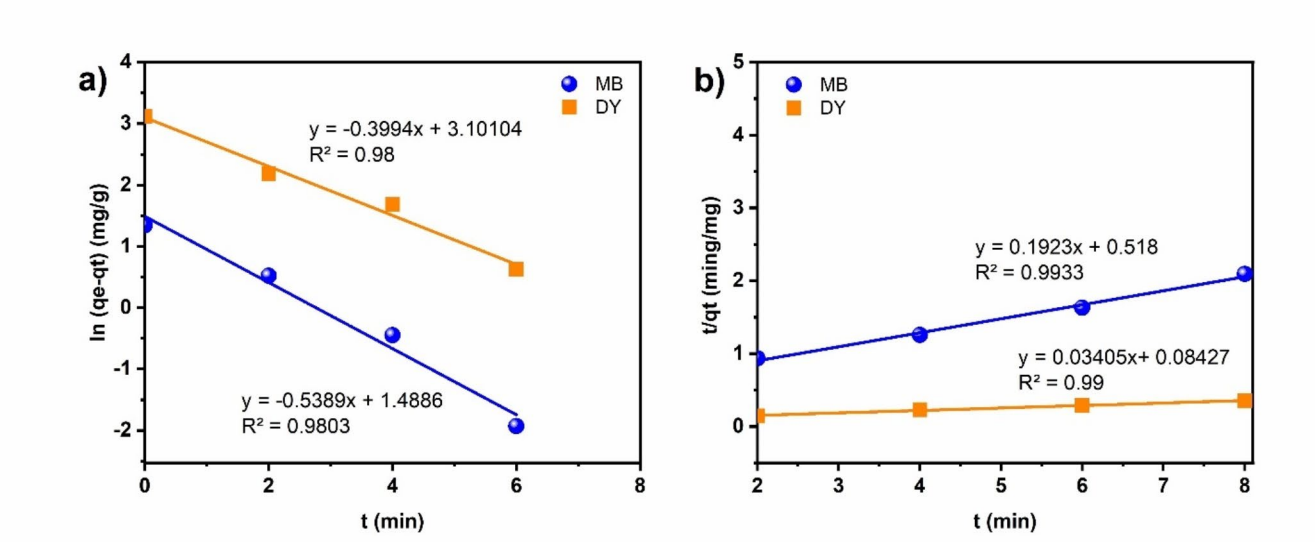

Fig. 12 **a** Pseudo-first order kinetic plot and **b** Pseudo-second order kinetic plot for the degradation of MB and DY

k_2, indicating a stronger chemical interaction between the adsorbent and DY than MB.

3.7 Photocatalysis Kinetics

Kinetic models are used to study the rate of the photocatalytic process and the potential rate-controlling phase. In this study, the kinetic data from batch trials have been evaluated using pseudo-first and pseudo-second-order models. This was accomplished by using 1.2 mg/mL and 0.6 mg/mL of photocatalyst, adjusting the pH of the solutions to 10.5 and 1 for MB and DY, respectively, and allowing for reaction times of 2, 4, 6, and 8 min.

According to Fig. 13, the pseudo-first-order correlation coefficient values (R^2) for first-order reactions are 0.99 for both dyes. Therefore, when comparing those models, the correlation coefficients obtained from the first-order model fit better than those for the second-order kinetics model, suggesting that pseudo-first-order kinetics was followed during the photodegradation process.

3.8 Photocatalytic Degradation of Synthetic Dye Effluent

The photocatalytic performance of PDAAQ polymer was also investigated in synthetic effluent solution (SES) environments prepared with chemicals typically found in textile effluents [79, 80]. To stimulate the synthetic wastewater (SWW), firstly, SES stock solution was prepared by adding 0.013 g starch, 0.0278 g sodium sulfate, and 0.028 g sodium phosphate into 1 L ultrapure water [79, 80]. The SES solution was stirred for 90 min at 80 °C. SWW was obtained with dissolving dyes in SES. The SES solutions containing MB and DY were named MB-SWW and DY-SWW, respectively. Moreover, to investigate the synergic effect of dyes, MB and DY dyes simultaneously dissolve in an SES medium with a molar ratio of 1:1 (MB + DY-SWW). The pH of the single dye solutions was adjusted to 10.5 for MB and 1 for DY (Fig. 8b). The pH of MB + DY-SWW was adjusted as pH 3 was the cut-off point of the curves in Fig. 8b.

Figure 14a shows the time-dependent change of the UV-vis absorbance spectrum of MB-SWW under visible light illumination in the presence of PDAAQ. MB-SWW was completely degraded after 12 min visible light illumination. At the same time, with the adsorption mechanism, MB-SWW decolorized 61.39% in the presence of PDAAQ under dark conditions.

The decrease of intensities of the characterization absorbance band of DY-SWW is given in Fig. 14b. The degradation efficiency of DY-SWW reached 78.3% after 12 min visible light irradiation in the presence of PDAAQ. Under dark conditions, DY-SWW decolorized as 25.5% after 12 min. Moreover, under 28 min visible light illuminations, the DY-SWW dye was completely degraded. The decreased degradation rate of MB-SWW and DY-SWW (solution prepared with SES) compared with model dye MB and DY (solution prepared with ultrapure water) may be attributed to the competitive adsorbance of ions [81]. Figure 14c indicates the change of the UV-vis absorbance spectrum of MB + DY-SWW under visible light illumination in the presence of PDAAQ. The UV-vis absorbance spectrum of

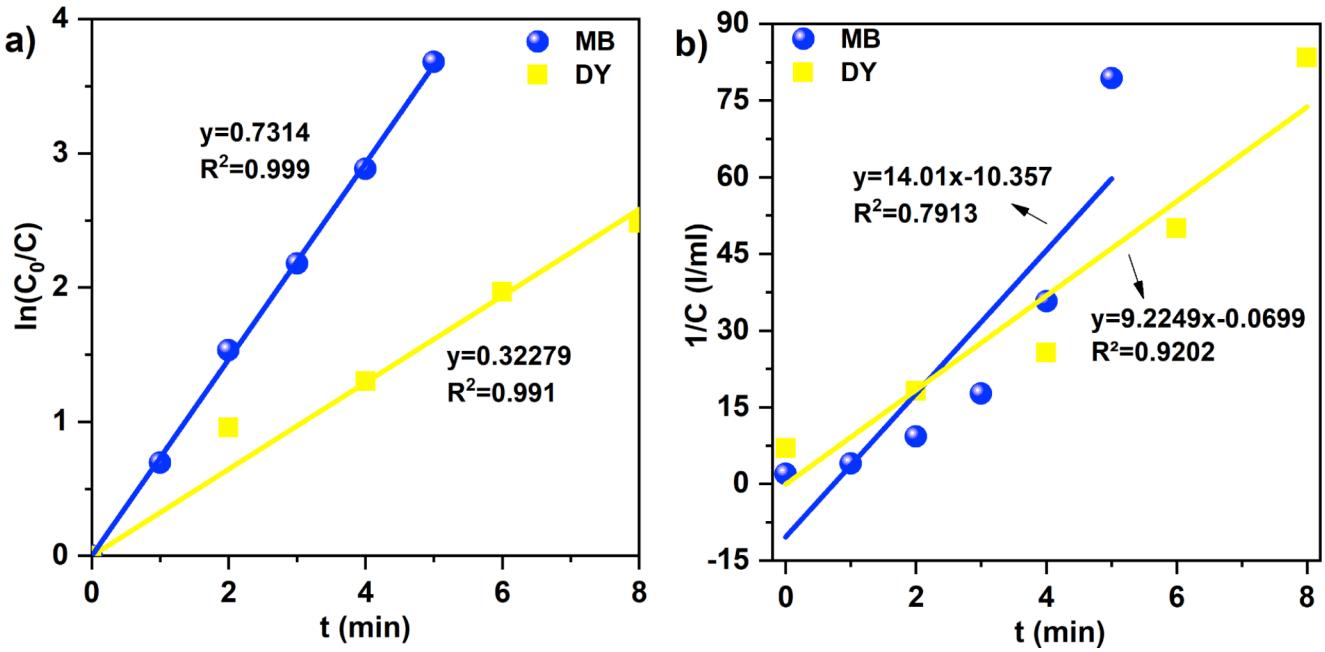

Fig. 13 The photocatalytic degradation of MB and DY under visible light is represented by the **a** first and **b** second-order kinetic models

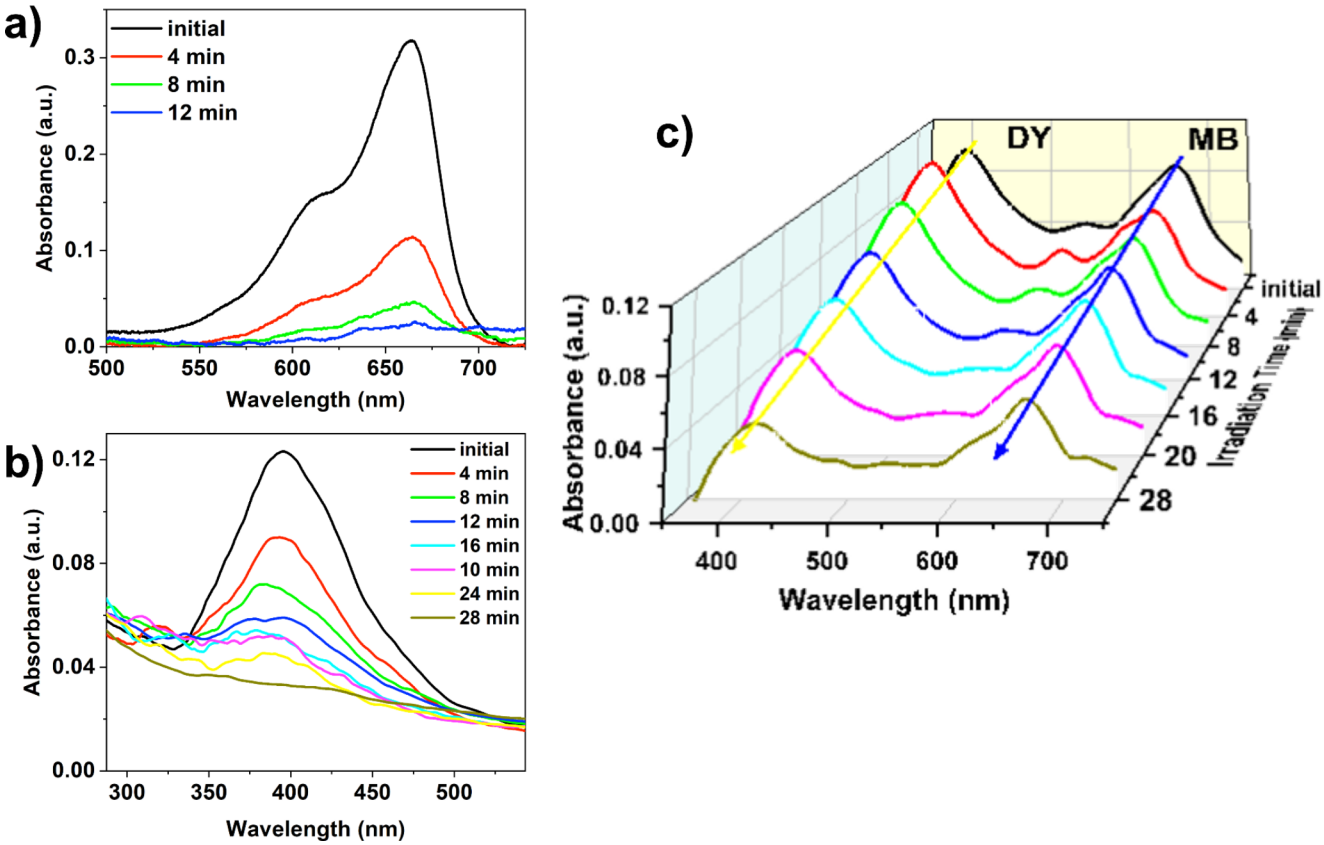

Fig. 14 Time-dependent UV-vis absorbance spectrum of **a** MB-SWW, **b** DY-SWW, and **c** MB + DY-SWW in the presence of PDAAQ under visible light irradiation (photocatalysts dosage: 0.4 mg/mL)

MB + DY-SWW contains the characteristic absorbance band of MB and DY. Under visible light illumination, the intensities of the characterization absorbance band of MB and DY dyes were simultaneously decreased. After 28 min visible light illumination, MB and DY dyes degraded as 49.3 and 44.3%, respectively. The degradation rate of the MB and DY mixture in SWW is lower than that of the single dye in SWW and model dyes prepared with ultrapure water. The decrease in the photocatalytic reaction rate of MB + DY-SWW can be attributed to the reaction of ions in SES with radical species involved in the photocatalytic mechanism. Also, potential competitive interactions between MB and DY dyes in the solution during adsorption and adsorption-assisted photocatalytic degradation mechanism, which may affect their access to active sites on the photocatalyst surface, ultimately leading to reduced photocatalytic efficiency for each dye when present in a mixed-dye system. Since the amount of photocatalyst was kept constant during these experiments, the degradation of each dye decreased compared to the case of the dyes alone.

4 Conclusion

The conductive PDAAQ polymer was synthesized with chemical oxidative polymerization using an oxidant/initiator system. Under visible light irradiation, the produced PDAAQ polymer exhibits exceptional photocatalytic activity because it absorbs UV, visible, and near-infrared regions of the absorbance spectrum. This study provided the first comprehensive evaluation of PDAAQ's photocatalytic capabilities, revealing its ability to completely degrade MB and DY dyes within 6 and 8 min, respectively, using an adsorption-assisted photocatalytic approach in the presence of 0.4 mg/ml photocatalyst. The degradation kinetics followed the Langmuir isotherm and pseudo-second-order models, suggesting monolayer adsorption and a chemisorption-controlled process. Scavenger experiments identified $\cdot O_2^-$ as the primary reactive species, supported by h + and ˙OH as secondary contributors.

Additionally, PDAAQ's applicability in real-world scenarios was assessed using synthetic wastewater. Complete dye degradation was achieved for individual dyes, while mixed dye systems maintained significant degradation efficiency. These findings suggest that the synthesized PDAAQ

demonstrates strong potential for practical application in real wastewater treatment with super photocatalytic performance where multiple dye contaminants are also present.

Supplementary Information The online version contains supplementary material available at https://doi.org/10.1007/s10904-025-03605-x.

Author Contributions Aleyna Akıllı: Investigation, formal analysis, data curation, writing-original draft (equal), Ayşenur Özler: Investigation, Bircan Haspulat Taymaz: Investigation, formal analysis, data curation, visualization, writing-original draft (equal), Ahmet Hancı: Investigation, Volkan Eskizeybek: investigation Handan Kamış: investigation, funding acquisition, writing-review&editing, supervision.

Funding Open access funding provided by the Scientific and Technological Research Council of Türkiye (TÜBİTAK).
This research study was supported by The Scientific and Technical Research Council of Turkey with the Project Code: 221M523 and Konya Technical University Scientific Research Projects under Grant number 201116020 and 232316064.

Data Availability No datasets were generated or analysed during the current study.

Declarations

Competing Interests The authors declare that they have no known competing financial interests or personal relationships that could have appeared to influence the work reported in this paper.

References

1. D. Zioui, P.M. Martins, L. Aoudjit et al., Wastewater treatment of real effluents by microfiltration using poly(vinylidene fluoride–hexafluoropropylene) membranes. Polymers (Basel) (2023). https://doi.org/10.3390/polym15051143
2. P.M. Martins, H. Salazar, L. Aoudjit et al., Crystal morphology control of synthetic giniite for enhanced photo-fenton activity against the emerging pollutant metronidazole. Chemosphere. (2021). https://doi.org/10.1016/j.chemosphere.2020.128300
3. B. Haspulat Taymaz, V. Eskizeybek, H. Kamış, PANI/CoO nanocomposite films with excellent photocatalytic performance for real textile wastewater treatment. Water Air Soil. Pollut. (2023). https://doi.org/10.1007/s11270-023-06575-3
4. K. Singh, R. Verma, A. Chauhan et al., Waste water treatment using piezoelectric materials: a review on piezo-photocatalysis. Top. Catal. **67**, 1101–1128 (2024). https://doi.org/10.1007/s11244-024-01966-0
5. A. Nishat, M. Yusuf, A. Qadir et al., Wastewater treatment: a short assessment on available techniques. Alexandria Eng. J. **76**, 505–516 (2023)
6. H.N. Tran, (2023) Adsorption technology for water and wastewater treatments. Water (Switzerland) **15**
7. D. Zioui, H. Salazar, L. Aoudjit et al., Polymer-based membranes for oily wastewater remediation. Polymers (Basel) (2020). https://doi.org/10.3390/polym12010042
8. L. Aoudjit, E.L. Amine Nebbat, D. Zioui, (2023) Chitosan/ZnO nanocomposite membranes for removal of paracetamol from water
9. A. Akıllı, B. Haspulat Taymaz, A. Özler et al., Magnetic and visible light-induced novel green synthesized magnetic Co_3O_4 photocatalysts via sunflower seed meal extract for anionic and cationic dye removal by adsorption assisted photocatalytic degradation. Int. J. Phytorem. (2024). https://doi.org/10.1080/15226514.2024.2416998
10. M. Salima, M. Youcef, T. Bouarroudj et al., Sunlight-assisted photocatalytic degradation of tartrazine in the presence of mg doped ZnS nanocatalysts. Solid State Sci. (2023). https://doi.org/10.1016/j.solidstatesciences.2023.107260
11. K.S. Randhawa, Photocatalytic degradation of pollutants using advanced ceramics: materials, mechanism, synthesis, and applications. J. Inorg. Organomet. Polym. Mater. (2024). https://doi.org/10.1007/s10904-024-03068-6
12. A. Azam, T. Iqbal, Efficient fabrication of Cu-doped TiO_2 nanoparticles for enhanced visible light photocatalysis and antimicrobial efficacy. J. Inorg. Organomet. Polym. Mater. (2024). https://doi.org/10.1007/s10904-024-03232-y
13. F. Saib, F.M. Laoui, L. Aoudjit et al., Physical and photo-electrochemical characterization of $Ca_2Fe_2O_5$ for metronidazole antibiotic degradation under sunlight. Opt. Mater. (Amst). (2024). https://doi.org/10.1016/j.optmat.2023.114806
14. L. Aoudjit, D. Zioui, F. Touahra et al., Photocatalytic degradation of tartrazine dyes using TiO_2–chitosan beads under sun light irradiation. Russ. J. Phys. Chem. A **95**, 1069–1076 (2021). https://doi.org/10.1134/S0036024421050034
15. V. Van Tran, T.T.V. Nu, H.R. Jung, M. Chang, (2021) Advanced photocatalysts based on conducting polymer/metal oxide composites for environmental applications. Polymers (Basel) **13**
16. S. Jadoun, U. Riaz, J. Yáñez, N. Pal Singh Chauhan, (2021) Synthesis, characterization and potential applications of poly(o-phenylenediamine) based copolymers and nanocomposites: a comprehensive review. Eur. Polym. J. **156**
17. M. Demir, B.H. Taymaz, M. Sarıbel, H. Kamış, Photocatalytic degradation of organic dyes with magnetically separable PANI/Fe_3O_4 composite under both UV and visible-light irradiation. ChemistrySelect (2022). https://doi.org/10.1002/slct.202103787
18. S.A. Ahire, A.A. Bachhav, B.S. Jagdale et al., Amalgamation of ZrO_2-PANI nanocomposite polymeric material: characterization and expeditious photocatalytic performance towards carbol Fuchsin (CF) dye and kinetic study. J. Inorg. Organomet. Polym. Mater. **33**, 1357–1368 (2023). https://doi.org/10.1007/s10904-023-02590-3
19. A. Ledezma-Espinoza, L. Rodríguez-Quesada, M. Araya-Leitón et al., Modified cellulose/poly(3,4-ethylenedioxythiophene) composite as photocatalyst for the removal of sulindac and carbamazepine from water. Environ. Technol. Innov. (2022). https://doi.org/10.1016/j.eti.2022.102483
20. B. Haspulat Taymaz, A novel Ppy/ZnO@Co ternary nanocomposite with enhanced visible light-driven photocatalytic performance. J. Taiwan. Inst. Chem. Eng. (2023). https://doi.org/10.1016/j.jtice.2023.104741

21. O.S. Adedoja, E.R. Sadiku, Y. Hamam, Prospects of hybrid conjugated polymers loaded graphene in electrochemical energy storage applications. J. Inorg. Organomet. Polym. Mater. **33**, 3915–3934 (2023)
22. T. Abdiryim, A. Ali, R. Jamal et al., (2014) A facile solid-state heating method for preparation of poly(3,4-ethelenedioxythiophene)/ZnO nanocomposite and photocatalytic activity
23. N. Ahmad, S. Sultana, S. Sabir, M.Z. Khan, Exploring the visible light driven photocatalysis by reduced graphene oxide supported Ppy/CdS nanocomposites for the degradation of organic pollutants. J. Photochem. Photobiol. Chem. (2020). https://doi.org/10.1016/j.jphotochem.2019.112129
24. B. Haspulat Taymaz, V. Eskizeybek, H. Kamış, A novel polyaniline/NiO nanocomposite as a UV and visible-light photocatalyst for complete degradation of the model dyes and the real textile wastewater. Environ. Sci. Pollut. Res. **28**, 6700–6718 (2021). https://doi.org/10.1007/s11356-020-10956-0
25. N. Sharma, A. Singh, N. Kumar et al., A review on polyaniline and its composites: from synthesis to properties and progressive applications. J. Mater. Sci. **59**, 6206–6244 (2024)
26. K. Bednarczyk, W. Matysiak, T. Tański et al., Effect of polyaniline content and protonating dopants on electroconductive composites. Sci. Rep. (2021). https://doi.org/10.1038/s41598-021-86950-4
27. S. Goswami, S. Nandy, E. Fortunato, R. Martins, Polyaniline and its composites engineering: a class of multifunctional smart energy materials. J. Solid State Chem. (2023). https://doi.org/10.1016/j.jssc.2022.123679
28. X.G. Li, H. Li, M.R. Huang, Productive synthesis and properties of polydiaminoanthraquinone and its pure self-stabilized nanoparticles with widely adjustable electroconductivity. Chem. Eur. J. **13**, 8884–8896 (2007). https://doi.org/10.1002/chem.200700541
29. K. Naoi, S. Suematsu, M. Hanada, H. Takenouchi, Enhanced cyclability of π–π stacked supramolecular (1,5-diaminoanthraquinone) oligomer as an electrochemical capacitor material. J. Electrochem. Soc. **149**, A472 (2002). https://doi.org/10.1149/1.1456920
30. K. Naoi, S. Suematsu, A. Manago, (2000) Electrochemistry of poly(1,5-diaminoanthraquinone) and its application in electrochemical capacitor materials
31. M.T.T. Nguyen, H.L. Nguyen, D.T. Nguyen, Poly(1,5-diaminonaphthalene)-modified screen-printed device for electrochemical lead ion sensing. Adv. Polym. Technol. (2021). https://doi.org/10.1155/2021/6637316
32. M. Gao, F. Yang, X. Wang et al., Electrochemical characteristics and stability of poly(1,5- diaminoanthraquinone) in acidic aqueous solution. J. Phys. Chem. C **111**, 17268–17274 (2007). https://doi.org/10.1021/jp074415j
33. I. Amer, D.A. Young, Chemically oxidative polymerization of aromatic diamines: the first use of aluminium-triflate as a co-catalyst. Polymers (Guildf) **54**, 505–512 (2013). https://doi.org/10.1016/j.polymer.2012.11.078
34. G. Zarren, B. Nisar, F. Sher, (2019) Synthesis of anthraquinone-based electroactive polymers: a critical review. Mater. Today Sustain, **5**
35. B. Haspulat-Taymaz, Görünür işik ile uyarilabilen Ppy/ZnO@Fe kompozitinin fotokatalitik aktivitesinin optimizasyonu. Konya J. Eng. Sci. **9**, 42–53 (2021). https://doi.org/10.36306/konjes.979621
36. B. Haspulat Taymaz, H. Kamiş, Ö. Yoldaş, Photocatalytic degradation of malachite green dye using zero valent iron doped polypyrrole. Environ. Eng. Res. (2022). https://doi.org/10.4491/eer.2020.638
37. F. Aoudjit, F. Touahra, L. Aoudjit et al., Efficient solar heterogeneous photocatalytic degradation of metronidazole using heterojunction semiconductors hybrid nanocomposite, layered double hydroxides. Water Sci. Technol. **82**, 2837–2846 (2020). https://doi.org/10.2166/wst.2020.519
38. S. Wong, N.A. Ghafar, N. Ngadi et al., Effective removal of anionic textile dyes using adsorbent synthesized from coffee waste. Sci. Rep. (2020). https://doi.org/10.1038/s41598-020-60021-6
39. N.S. Jamaluddin, N.H. Alias, S. Samitsu et al., Efficient chromium (VI) removal from wastewater by adsorption-assisted photocatalysis using MXene. J. Environ. Chem. Eng. (2022). https://doi.org/10.1016/j.jece.2022.108665
40. H. Jain, A. Joshi, C.N. Ramachandran, R. Kumar, Synthesis of a highly efficient multifunctional copper (II)-pyridyl complex for adsorption and photocatalytic degradation of organic dyes. ChemistrySelect **4**, 4952–4961 (2019). https://doi.org/10.1002/slct.201900498
41. H.N. Tran, Applying linear forms of pseudo-second-order kinetic model for feasibly identifying errors in the initial periods of time-dependent adsorption datasets. Water (Switzerland) (2023). https://doi.org/10.3390/w15061231
42. N.A. Jasim, S.E. Ebrahim, S.H. Ammar, Photocatalytic degradation of rhodamine B using $Co_xZn_{1-x}Fe_2O_4$ nanocomposite under visible light irradiation: synthesis, characterization and its application. Alexandria Eng. J. **82**, 557–576 (2023). https://doi.org/10.1016/j.aej.2023.09.081
43. L. Aoudjit, P.M. Martins, F. Madjene et al., Photocatalytic reusable membranes for the effective degradation of tartrazine with a solar photoreactor. J. Hazard. Mater. **344**, 408–416 (2018). https://doi.org/10.1016/j.jhazmat.2017.10.053
44. N. An, W. Li, Z. Shao et al., Graphene oxide coated polyaminoanthraquinone@MXene based flexible film electrode for high-performance supercapacitor. J. Energy Storage. (2023). https://doi.org/10.1016/j.est.2022.106180
45. R. Maher, Z. Khalifa, A.A. Hathoot, M.A. Azzem, A novel electrochemical sensor based on poly(1,5-diaminonaphthalene) and poly(1,2-diaminoanthraquinone) core-shell composite electrodes for effective voltammetric determination of nitrite. Electroanalysis (2023). https://doi.org/10.1002/elan.202200225
46. N. An, L. Zhou, W. Li et al., Multifunctional polymer coating cooperated with γ-Fe_2O_3 for boosting photoelectrochemical water oxidation. Appl. Catal. B (2022). https://doi.org/10.1016/j.apcatb.2022.121869
47. N. An, Z. Shao, Z. Guo et al., High energy-density supercapacitor based on a novel conjugated poly (1, 5-diaminoanthraquinone)/intercalated graphene composite system. J. Power Sources (2020). https://doi.org/10.1016/j.jpowsour.2020.228692
48. A. Mostafaei, A. Zolriasatein, Synthesis and characterization of conducting polyaniline nanocomposites containing ZnO nanorods. Progress Nat. Sci.: Mater. Int. **22**, 273–280 (2012). https://doi.org/10.1016/j.pnsc.2012.07.002
49. J. Liu, P. Liu, Synthesis and electrochemical properties of various dimensional poly(1,5-diaminoanthraquinone) nanostructures: nanoparticles, nanotubes and nanoribbons. J. Colloid Interface Sci. (2019). https://doi.org/10.1016/j.jcis.2019.01.120
50. Y.O. Mezhuev, Y.V. Korshak, Theory of chain growth in chemical oxidative polymerization of aniline derivatives. Synth. Met. (2020). https://doi.org/10.1016/j.synthmet.2020.116445
51. R.P. Singh, A. Tiwari, A.C. Pandey, Silver/polyaniline nanocomposite for the electrocatalytic hydrazine oxidation. J. Inorg. Organomet. Polym. Mater. **21**, 788–792 (2011). https://doi.org/10.1007/s10904-011-9554-y
52. M. Beygisangchin, S.A. Rashid, S. Shafie et al., Preparations, properties, and applications of polyaniline and polyaniline thin films—a review. Polymers (Basel) (2021). https://doi.org/10.3390/polym13122003
53. T.A. Tikish, A. Kumar, J.Y. Kim, Electrical and optical properties of polypyrrole and polyaniline blends. Polym. Sci. - Ser. A **62**, 680–690 (2020). https://doi.org/10.1134/S0965545X20330056

54. N. Su, Improving electrical conductivity, thermal stability, and solubility of polyaniline-polypyrrole nanocomposite by doping with anionic spherical polyelectrolyte brushes. Nanoscale Res. Lett. (2015). https://doi.org/10.1186/s11671-015-0997-x
55. D. Li, H. Song, X. Meng et al., Effects of particle size on the structure and photocatalytic performance by alkali-treated TiO_2. Nanomaterials (2020). https://doi.org/10.3390/nano10030546
56. S.J. Tang, A.T. Wang, S.Y. Lin et al., Polymerization of aniline under various concentrations of APS and HCl. Polym. J. **43**, 667–675 (2011). https://doi.org/10.1038/pj.2011.43
57. L. Zhou, Z. Xu, D. Song et al., Improved film morphology and reduced defects in solution-processed red phosphorescent emission layer of the organic light-emitting diodes. Synth. Met. (2020). https://doi.org/10.1016/j.synthmet.2020.116322
58. C.B. Anucha, I. Altin, Z. Biyiklioglu et al., Synthesis, characterization, and photocatalytic evaluation of manganese (iii) phthalocyanine sensitized znwo4 (znwo4mnpc) for bisphenol a degradation under Uv irradiation. Nanomaterials. **10**, 1–24 (2020). https://doi.org/10.3390/nano10112139
59. P. Zhang, M. Sun, J. Liang et al., pH-modulated oxidation of organic pollutants for water decontamination: a deep insight into reactivity and oxidation pathway. J. Hazard. Mater. (2024). https://doi.org/10.1016/j.jhazmat.2024.134393
60. S.D. Khairnar, V.S. Shrivastava, Facile synthesis of nickel oxide nanoparticles for the degradation of methylene blue and rhodamine B dye: a comparative study. J. Taibah Univ. Sci. **13**, 1108–1118 (2019). https://doi.org/10.1080/16583655.2019.1686248
61. Y. Dai, J. Li, D. Shan, Adsorption of tetracycline in aqueous solution by biochar derived from waste *Auricularia auricula* dregs. Chemosphere (2020). https://doi.org/10.1016/j.chemosphere.2019.124432
62. A. Safri, A.J. Fletcher, R. Safri, H. Rasheed, Integrated adsorption–photodegradation of organic pollutants by carbon xerogel/titania composites. Molecules (2022). https://doi.org/10.3390/molecules27238483
63. N. Kumaresan, M.M.A. Sinthiya, K. Ramamurthi et al., Visible light driven photocatalytic activity of ZnO/CuO nanocomposites coupled with rGO heterostructures synthesized by solid-state method for RhB dye degradation. Arab. J. Chem. **13**, 3910–3928 (2020). https://doi.org/10.1016/j.arabjc.2019.03.002
64. H. Piao, J. Zhao, S. Zhang et al., Polypyrrole/cadmium sulfide/nickel hollow fiber as an enhanced and recyclable intrinsic photocatalyst for pollutant removal and high-effective hydrogen evolution. Int. J. Hydrogen Energy. **52**, 173–189 (2024). https://doi.org/10.1016/j.ijhydene.2022.11.286
65. A. Yar, B. Haspulat, T. Üstün et al., Electrospun TiO_2/ZnO/PAN hybrid nanofiber membranes with efficient photocatalytic activity. RSC Adv. **7**, 29806–29814 (2017). https://doi.org/10.1039/c7ra03699j
66. J. Zia, F. Fatima, U. Riaz, A comprehensive review on the photocatalytic activity of polythiophene-based nanocomposites against degradation of organic pollutants. Catal. Sci. Technol. **11**, 6630–6648 (2021)
67. X. Wang, X. Li, B. Li et al., Surface-reconstructed FeOOH@CoFeOS/NF architectures: leveraging nano-layered stacking for accelerated oxygen evolution kinetics. New J. Chem. (2025). https://doi.org/10.1039/D4NJ04690K
68. M. Khan, S.W. Ali, M. Shahadat, S. Sagadevan, Applications of polyaniline-impregnated silica gel-based nanocomposites in wastewater treatment as an efficient adsorbent of some important organic dyes. Green. Process. Synth. **11**, 617–630 (2022)
69. T. Bouarroudj, L. Aoudjit, L. Djahida et al., Photodegradation of tartrazine dye favored by natural sunlight on pure and (ce, Ag) co-doped ZnO catalysts. Water Sci. Technol. **83**, 2118–2134 (2021). https://doi.org/10.2166/wst.2021.106
70. H. Katsumata, M.A. Islam Molla, J.B. Islam et al., Dual Z-scheme heterojunction g-C_3N_4/Ag_3PO_4/AgBr photocatalyst with enhanced visible-light photocatalytic activity. Ceram. Int. **48**, 21939–21946 (2022). https://doi.org/10.1016/j.ceramint.2022.04.176
71. Ş Parlayici, Alginate-coated perlite beads for the efficient removal of methylene blue, malachite green, and methyl violet from aqueous solutions: kinetic, thermodynamic, and equilibrium studies. J. Anal. Sci. Technol. (2019). https://doi.org/10.1186/s40543-019-0165-5
72. Y. Wu, F. Wang, X. Jin et al., Highly active metal-free carbon dots/g-C_3N_4 hollow porous nanospheres for solar-light-driven PPCPs remediation: mechanism insights, kinetics and effects of natural water matrices. Water Res. (2020). https://doi.org/10.1016/j.watres.2020.115492
73. S. Abuzerr, M. Darwish, A.H. Mahvi, Simultaneous removal of cationic methylene blue and anionic reactive red 198 dyes using magnetic activated carbon nanoparticles: equilibrium, and kinetics analysis. Water Sci. Technol. **2017**, 534–545 (2017). https://doi.org/10.2166/wst.2018.145
74. T.M.P.D.M. Thennakoon, A.P.G.M.V. Samaraweera, N. Priyantha, Adsorption of Cr(III) from aqueous solution on NaOH-treated scraped coconut waste. Ceylon J. Sci. **50**, 391–401 (2021). https://doi.org/10.4038/cjs.v50i5.7928
75. N. Al-Afy, H. Sereshti, Rapid removal of boron from environmental water samples using magnetic graphene oxide: optimized by central composite design. Desalin. Water Treat. **153**, 65–75 (2019). https://doi.org/10.5004/dwt.2019.23948
76. M.S. Mohy Eldin, K.M. Aly, Z.A. Khan et al., Removal of methylene blue from synthetic aqueous solutions with novel phosphoric acid-doped pyrazole-g-poly(glycidyl methacrylate) particles: kinetic and equilibrium studies. Desalin. Water Treat. **57**, 27243–27258 (2016). https://doi.org/10.1080/19443994.2016.1171168
77. I.M. Minisy, N.A. Salahuddin, M.M. Ayad, Adsorption of methylene blue onto chitosan–montmorillonite/polyaniline nanocomposite. Appl. Clay Sci. (2021). https://doi.org/10.1016/j.clay.2021.105993
78. T.A. Aragaw, A.N. Alene, A comparative study of acidic, basic, and reactive dyes adsorption from aqueous solution onto kaolin adsorbent: effect of operating parameters, isotherms, kinetics, and thermodynamics. Emerg. Contam. **8**, 59–74 (2022). https://doi.org/10.1016/j.emcon.2022.01.002
79. M.A. Rafique, A. Jamal, G. Afzal et al., Photocatalytic mediated remediation of synthetic dyes effluent using zero-valent iron: a comparative study. Desalin. Water Treat. **237**, 284–291 (2021). https://doi.org/10.5004/dwt.2021.27723
80. D.A. Yaseen, M. Scholz, Treatment of synthetic textile wastewater containing dye mixtures with microcosms. Environ. Sci. Pollut. Res. **25**, 1980–1997 (2018). https://doi.org/10.1007/s11356-017-0633-7
81. S. Satyam, S. Patra, Innovations and challenges in adsorption-based wastewater remediation: a comprehensive review. Heliyon (2024). https://doi.org/10.1016/j.heliyon.2024.e29573